공학박사 학위논문

Studies on Green-sensitive Organic Optoelectronic Materials with High Spectral Sensitivity and Frequency Response for the Application of CMOS Image Sensors

CMOS 이미지 센서 응용을 위해 우수한 파장 선택적 감도와 응답특성을 갖는 녹색 감지형 유기 광전재료에 관한 연구

2015년 2월

서울대학교 대학원

재료공학부

이 광 희

Studies on Green-sensitive Organic Optoelectronic Materials with High Spectral Sensitivity and Frequency Response for the Application of CMOS Image Sensors

A THESIS SUBMITTED IN PARTIAL FULFILLMENT OF
THE REQUIREMENTS FOR THE DEGREE OF
DOCTOR OF PHILOSOPHY
IN ENGINEERING AT THE GRADUATE SCHOOL OF
SEOUL NATIONAL UNIVERSITY

FEBRUARY 2015

By

Kwang-Hee Lee

Supervisor

Prof. Soo Young Park

Abstract

Studies on Green-sensitive Organic Optoelectronic Materials with High Spectral Sensitivity and Frequency Response for the Application of CMOS Image Sensors

Lee Kwang-Hee

Department of Materials Science and Engineering

The Graduate School

Seoul National University

The progresses in photodetector technology, converting light into electric signal, has boosted up the development of various fields, for example in medicine imaging with x-ray detector, in the military and security domains with infrared sensors, or in image processing with sensors for the visible range. Conventional silicone-based photodiodes (Si PD) used in complementary metal oxide semiconductor (CMOS) image sensors have led the imaging technology market thanks to their high photo-electric conversion efficiency and low dark currents. However, their low absorption coefficient and broad absorption in the visible region require thick photodiodes with additional image processing systems, which might restrict their high

sensitivity and ultra-high resolution.

Organic semiconductor materials that selectively absorb visible colors with a high absorption coefficient are promising material candidates to replace silicon in PD, making obsolete the use of color filters. In particular, green-sensitive organic photodetectors (OPD) can be integrated into a stacked PD on the Si-based blue and red PDs, which might lead to a significant increase in the sensitivity because of the doubled sensing area. This thesis therefore focuses on the development and characterization of new green-sensitive organic small molecules for CMOS image sensors applications. To date, fullerene has been the material of choice for acceptor materials in most OPDs because of its high electron mobility. However, fullerene is not the ideal material for green-selective OPDs due to its absorption characteristics in the blue range of the visible spectrum. Non-fullerene donor and acceptor materials with narrower absorption band widths are still needed.

In this regard, this dissertation addresses the following three topics: i) high performing non-fullerene small molecules for donor/acceptor bulk-heterojunction (BHJ) OPD devices, ii) spectral sensitivity and color crosstalk with these organic materials, and iii) dynamic characterization of frequency response based on their molecular structure.

In chapter II, fullerene-free BHJ OPD with high efficiency and green-color

selectivity are presented. It is demonstrated that, by choosing *N*,*N*-dimethyl quinacridone (DMQA) as a donor and dibutyl-substituted dicyanovinyl-terthiophene (DCV3T) as an acceptor, a maximum external quantum efficiency (EQE) of larger than 67 % at 540 nm could be achieved at -5 V bias. The overall OPD device performance, including the electrical and optical response, as well as the charge carrier generation and charge transport characteristics are discussed. In particular it is shown that the material compositions rich in DMQA exhibited a high yield of photogenerated charge carriers and a low absorption intensity, whereas the compositions rich in DCV3T had a high absorption intensity and low yield of charge carriers. A 1:1 ratio is optimal for device performance as a result of the relatively high absorption and efficient photogeneration of the charge carriers. This composition ensures the balance between electron and hole mobilities, which is essential to enhance the EQE.

Chapter III focuses on green-sensitive OPDs with high sensitivity and spectral selectivity, which employ boron subphthalocyanine chloride (SubPc) derivatives as either the donor or acceptor material. A maximum EQE of 62.6 % at an applied voltage of -5 V is achieved by combining SubPc with DCV3T, at the value of a large full-width-at-half-maximum (FWHM) of 211 nm, however. Considering spectral selectivity, the optimized performance is obtained by combining DMQA and SubPc with a high specific detectivity (D^*) of 2.34×10^{12} cm $Hz^{1/2}$/W, an EQE

value of 60.1% at -5 V and a narrow FWHM of 131 nm. It is further shown that, in spite of the sharp absorption of SubPc at the maximum wavelength (λ_{max}) of 586 nm, the EQE spectrum is smooth and favorably centered in the green region at λ_{max} of 560 nm, assisted by the high reflectance of SubPc centered at 605 nm. The photoresponsivity of the OPD devices is found to be consistent with their absorptance. With this DMQA / SubPc composition, promising green-sensitive OPD device are finally obtained, which is characterized by low value blue crosstalk (0.42) and moderate red crosstalk (0.37).

In chapter IV, the dynamic characterization of two high performing green-sensitive OPDs introduced in chapter II and III is further investigated by analyzing the electrical parameters based on experimental and simulation data. The two OPDs comprise DMQA as the common donor and DCV3T or SubPc as the respective acceptors. At the applied voltage of -5 V, the device composed of DMQA/SubPc shows a higher frequency response at 148.3 kHz, by 55 kHz higher than the device based on DMQA/DCV3T. The impedance spectroscopic results indicate that the former device exhibits the lower resistance due to the higher mobility and the lower capacitance attributed to the lower dielectric constant. The calculated reorganization energy and polarizability of these two different acceptors, which are theoretical parameters related to charge mobility and dielectric constant, are consistent with the experimental results. The OPD device comprising SubPc, with

the dynamic response surpassing the commercialization level of 100 kHz, is presented as an interesting candidate for potential applications as image sensors, together with its good static performance with external quantum efficiency of 60.1 % at the wavelength of 540 nm.

The specific approach toward green-sensitive OPDs elaborated in this dissertation, presented sequentially in Chapter II, III, and IV, can serve as a guideline for developing the blue- or red-sensitive OPDs.

KEYWORDS: CMOS image sensor, Organic photodetector, Organic semiconductor, Spectral sensitivity, Frequency response

Student Number: 2005-31024

Contents

List of Tables

List of Figures

CHAPTER I.
Introduction

The image recognition function of the human eyes is a sequential process transforming visible colors to an electrical signal. Aside from bio-mimetic technology, the organic opto-electronic technology has been recently expanding up to the commercialization of organic light emitting diodes (OLEDs) and organic photovoltaic cells (OPVs). In the field of image detection, highly sensitive organic photodetectors (OPDs) using polymeric semiconductor materials, representing a much more cost-effective approach as compared to inorganic technology, have been extensively tested in various configurations.[1]

Despite the advantages mentioned above, conventional image sensors installed in mobile electronic devices with high resolution and low noise level are based on complementary metal oxide semiconductor (CMOS) circuits with Si photodetectors (PDs), which exhibit the combined advantages of high photo-electric conversion efficiency with low dark current.[2] However, the inherent properties of Si PD such as non-selective color sensitivity in the visible region and low absorption coefficient are not optimal, necessarily demanding an additional color separation systems resulting in thick photodiode devices.[3]

Organic semiconductor materials, because of selective absorption of visible color with

high absorption coefficient, can be the promising alternative to replace Si-PDs and color-filters. Recently, many researchers have reported on the photo-response of organic materials for the different areas of the light spectrum, and on their related device physics.[1,4-6] Considering the state of the arts, it appears that the development of green-sensitive OPDs is urgently needed for the formation of highly efficient double decker OPD comprising the green-OPD overlayer and the blue- and red-PD bottom layer constructed in the Si substrate.

This chapter begins with a brief summary on organic semiconductor materials for light sensing classified by their different absorption wavelength range. Then, the basic electrical properties of OPDs applied to the image detection are introduced. Finally, the green-sensitive small molecule compounds used in this study and the research objectives are explained.

I.1. Organic photodetector (OPD) for light sensing

I.1.1. Photodetection for ultra-violet, visible and infra-red regions[1,5-6]

The sensing spectral region of photodetectors is critical for a variety of industrial and scientific applications, for examples for environmental monitoring, communications, remote control, day- and night-time surveillance, and chemical/biological sensing.[6]

The absorption wavelength range (λ) of an organic semiconductor material is governed by the energy bandgap (E_g) between the highest occupied molecular orbital (HOMO) and lowest unoccupied molecular orbital (LUMO). The light spectrum is divided in UV light (λ< 400 nm, E_g > 3.1 eV), visible light (400 - 700 nm) and IR light (λ> 700 nm, E_g<1.7 eV) including broad-band detection. The photo-response of semiconductor materials with various spectral regions is shown in Figure I-1.[6]

Ultra-violet (UV) detection: UV photodetectors are generally applied to visible-blind domains such as space communications, flame and chemical sensing, and medical devices.

Small molecules are quite common materials adopted for the UV responsive layer, preferentially deposited by vacuum thermal evaporation. As a donor material, 4,4′,4″-tri-(2-methylphenyl- phenylamino) triphenylaine (m-MTDATA) has been widely used because of its relatively high hole mobility of 3×10^{-5} cm^2 /Vs, a very low electron affinity (E_A) of 1.9 eV and an ionization potenital (I_P) of 5.1 eV.[7] The m-MTDATA has been combined with 8-hydroxyquinoline-based compounds as acceptor.

Among them, tris(8-hydroxyquinoline) aluminum (Alq_3) and tris(8-hydroxyquinoline) gallium (Gaq_3) show similar energy levels, but Gaq_3 might additionally suppress radiative decay in combination with m-MTDATA. The m-MTDATA:Gaq_3 blend device

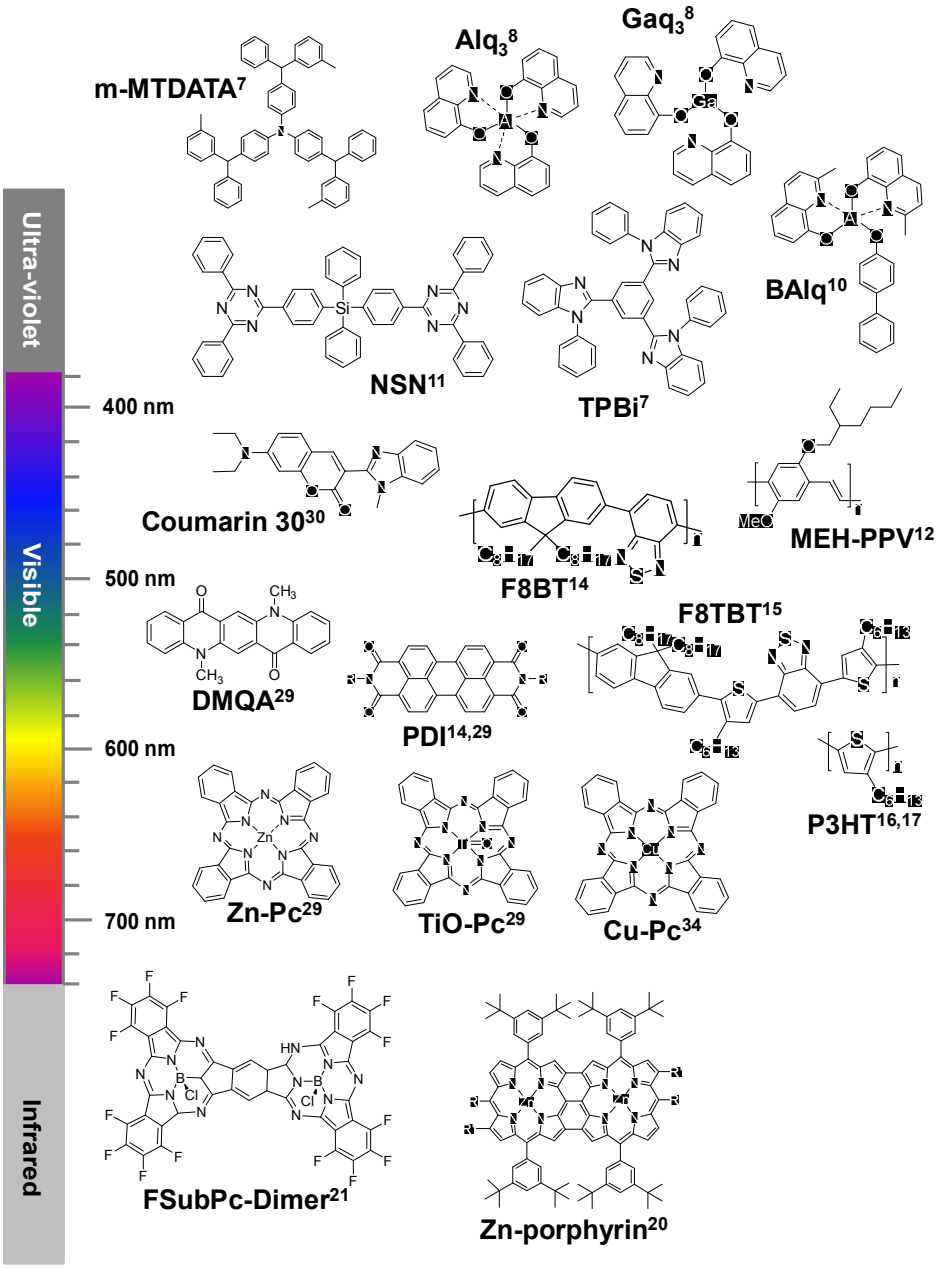

Figure I-1. Organic semiconductor molecules with the spectra from the UV to the NIR range. (Superscripts are the number of bibliographies.)

showed R = 338 mA/W at 365 nm, with an applied bias voltage of 8 V.[8] Both m-MTDATA:Alq_3 and m-MTDATA:Gaq_3 based device are not visible-blind due to a relatively strong absorption in the 400 to 450 nm range. To reduce absorption in the visible range, the Ga coordinating metal atom was substituted by various rare earth complexes, for example gadolinium, characterized by a blue-shifted absorption.[9] A detector with a 1:1 blend of m-MTDATA and tris-(8-hydroxyquinoline) gadolinium (Gdq) showed the responsivity of 230 mA/W at 7.5 V (EQE ≈ 78%) with a nearly suppressed photocurrent above 400 nm.

Additionally, some acceptor materials with a good energy level match to m-MTDATA have been reported, such as bis(2-methyl-8-quinolinato)-4-phenylphenolate aluminum (BAlq),[10] 1,3,5-tris(N-phenylbenzimidazol-2-yl) benzene (TPBi) with a high electron mobility,[7] a silane-containing triazine derivative (NSN) with good thermal stability and deep UV absorption.[11]

Visible detection: Organic photodetectors using visible-detective materials are continuously improved for applications to wide-use devices in our daily life such as image sensor, and to take advantage of the great flexibility of organic materials.[12] Ng *et al.* have demonstrated a flexbible image sensor array, as shown in Figure I-2a, using poly[2-methoxy-5-(2-ethylhexyloxy)-1,4-phenylene-vinylene] (MEH-PPV) and [6,6]-phenyl-C61-butyric acid methyl ester ($PC_{61}BM$) on a flexible substrate by inkjet

printing method. The OPD exhibited an EQE of 35 % at the bias voltage of -4 V and dark current under 1 nA/cm^2 with a BHJ structure. To enhance the performance in the overall visible region, excellent semiconducting polymers earlier developed for OPVs have been introduced; MEH-PPV,[12] poly(2-methoxy-5-(3'-7'-dimethyloctyloxy)-1,4-phenylenevinylene) (MDMO-PPV)[13] and 9,9'-dioctylfluorene-co-benzothiadiazole (F8BT)[14] as donors and poly([9,9-dioctylfl uorene]-2,7-diyl-alt-[4,7-bis(3-hexylthien-5-yl)-2,1,3-benzothiadiazole]-2,2,-diyl) (F8TBT)[15] and perylene diimides (PDI) derivatives[14] as acceptors. In case of polymer acceptors, promising alternative candidates to fullerenes have been suggested, because of their high electron affinity, electron mobility and solubility.

However, the composition poly(3-hexylthiophene) (P3HT) and $PC_{61}BM$, because of well characterized materials, have been often chosen owing to broad absorption between 400 and 600 nm with peak EQE above 70 %.[16] In particular, OPDs fabricated by spray-coating exhibited reproducible electrical properties with a low dark current density around 65 nA/cm^2 and a high EQE of 76 % at -5 V reverse bias.[17] Further study demonstrated the possibility to fabricate a hybrid CMOS-imager showing monochromatic images in 30 × 30 pixel array, as presented in Figure I-2c ~ I-2e.[18] To the P3HT:PCBM systems, squaraine (SQ) dyes were also added to enhance the near infra-red (NIR) absorption.

In contrast to polymers, small molecules have not been deeply investingated for overall

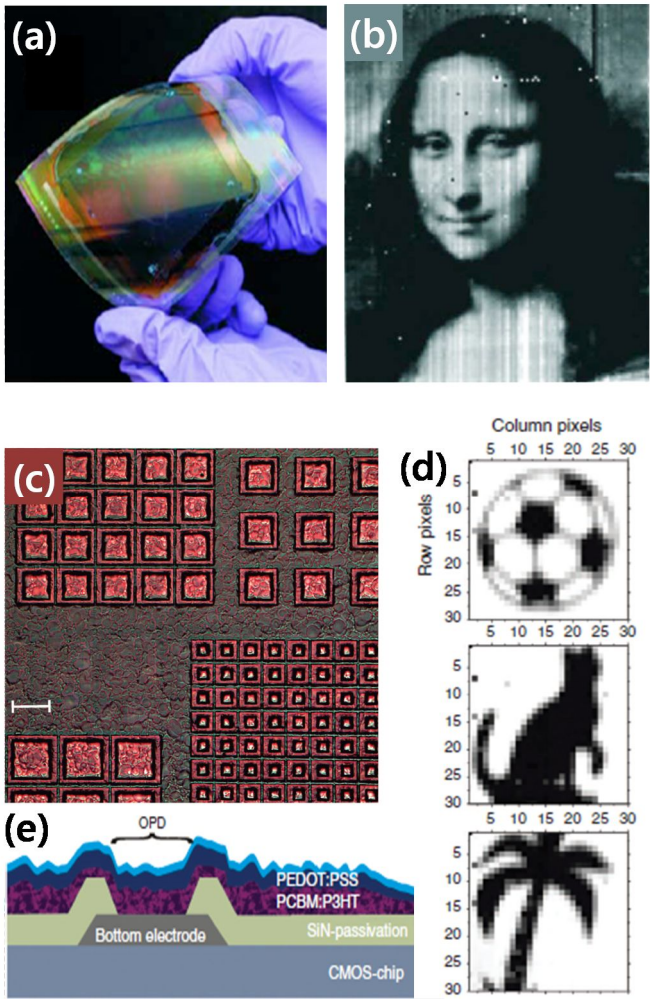

Figure I-2. Imager arrays and images for visible detection. (a) Flexible imager array using MEH-PPV:PCBM as a donor and an acceptor patterned by inkjet lithography on polyethylene naphthalate substrate, and (b) a projected image captured by the flexible image sensor array.[12] (c) The top view of the hybrid imager arrays using P3HT:PCBM blend with pixels of different sizes and pitches, (d) the monochromatic images accquired by 30 × 30 pixel array, and (c) the side view of the layer structure on the CMOS-chip.[18]

visible detection due to relative narrow absorption specta and to their poor solubility that limited their deposition by liquid coating. Their narrow absorption is however an advantage for the development of color-sensitive OPDs, which will be introduced in the next section I.1.2.

Infrared (IR) and broad-band detection: IR detection is also visible-blind, but relatively less harmful to human in comparison to UV. Therefore, IR detection has used in the fields of environmental monitoring, remote sensing and control and night-time observation. Materials with a low E_g of about 1.5 eV are sensitive to the IR or NIR regions. For example, Squaraine dyes with a broad absorption between 600 nm and 900 nm has been chosen as donor in IR OPD in combination with PCBM. An optimized performance of 3.5 % EQE at 670 nm was obtained for a 1:3 blend ratio, as a result of a well mixed morphology ensuring the good balance between holes and electrons mobilities.[19] As other candidates, two Zn-metallated porphyrins characterized by an absorption from the visible to the NIR regions with Q-band absorption peaks between 1050 nm and 1350 nm were also tested. For the best detector, a EQE peak of 6.5 %, a detectivity (D^*) of (2.3±0.1) × 10^{10} jones, and a response time of 2.12±0.02 ns at the wavelength of 1350 nm were achieved.[20] The fused dimer molecule exhibits a red-shifted and broader absorption as compared to the monomer because of extended π-conjugation.[21]

Another approach for efficient IR detection is the addition of colloidal quantum dots (CQD) allowing band-gap tunability because of the quantum size effect. Rauch *et al.*[22] demonstrated PbS-QD sensitized P3HT:PCBM detectors integrated on an a-Si TFT panel substrate with 256 × 256 pixels. The illustrative image under IR illumination at a wavelength of 1310 nm is presented in Figure I-3. Solution-processed photodetectors containing CQD showed excellent detectivity values up to 5×10^{13} jones, which is comparable to the best value reported for single-crystal photodiodes.[23]

These wide band-gap organic materials with CQD sensitization could be also adapted to broad-band detection, which is required in the fields of medical image sensing, telecommunications and environmental monitoring.[5,23]

I.1.2. Color sensing for CMOS image sensors

The color selective photo-detection properties of organic semiconductors in the visible region has been applied to advanced researches like artificial devices mimicking human eyes[24,25] and industrial colorimetric measurements.[26] For currently used applications, many researches focused on the replacement of Si-PDs and color-filters in conventional image sensors. These color-sensitive OPDs are adapted to sequential stacking for successive blue- (B), green- (G), and red- (R) absorption on a substrate, which might enhance the sensitivity. The concept on a stacked image sensor was

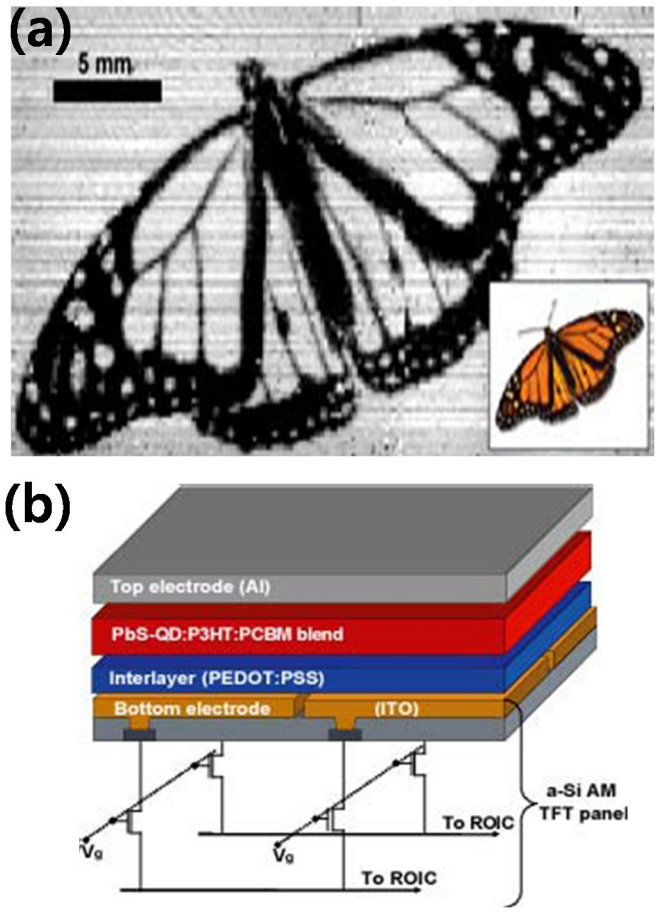

Figure I-3. Pbs-QD sensitized P3HT:PCBM OPD for NIR imaging. (a) Infrared shadow cast at 1310 nm of a slide showing a monarch butterfly (Inset: the original slide), and (b) schematic of the image structure with an a-Si TFT backplane.[22]

already issued as the patent in 2001.[27] Seo and Aihara *et al.* pursued and improved this approach for stacked color image sensor with B-, G-, R-sensitive OPDs.[28-33] At first, G-OPD with a *N,N'*-dimethylquinacridone / a perylene-diimide derivative and R-OPDs with Zn-phthalocyanine (ZnPc) / titanyl phthalocyanine (TiOPc) showed the EQEs of 7 % at 3 V and 18 % at 15 V.[29] And then, B-OPD exhibited an EQE of 64 % at the reverse bias of 10 V using C_{60}-doped Coumarin 30/Alq_3 in a planar heterojunction.[30] To verify the principle of stacked color imaging, they respectively tested three distinct B-, G- and R-organic layers with an amorphous In-Ga-Zn-O (IGZO) TFT array as a signal readout circuit on a glass substrate, and then stacked all elements to produce a test image sensor.[32] This concept is schematically represented Figure I-4a, and the normalized spectral photoresponse of the respective organic layers and the produced video image are shown in Figure I-4b[31] and I-4c,[33] respectively. In other studies on stacked image sensor, a red-sensitive OPD based on CuPc/C60 showing the EQE of 52 % at 620 nm and a specific detectivity of 4.0×10^{11} $cmHz^{1/2}/W$ was reported.[34] To reduce the blue-signal, two functional layers, a thick blue-absorbing layer and a thin wide band-gap layer as a barrier between a blue-aborbing layer and the photoactive layer, were added to the OPD. This approach was only adapted to red-OPD, because of the bottom position of the red-OPD in stacked sequence.

However, a full organic stacked image sensor has not been realized yet due to additional difficulties on process integration such as low temperature metallization and

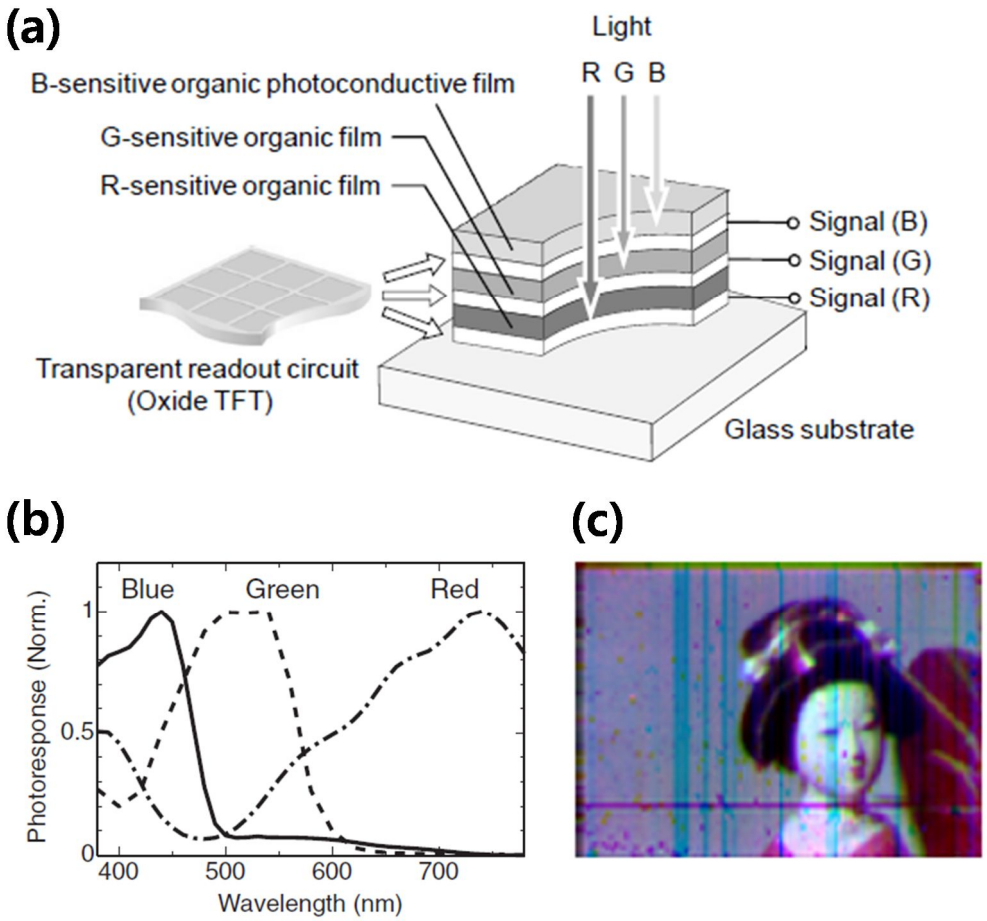

Figure I-4. The color-sensitive organic image sensor with a stacked structure. (a) Schematic concept of stacked organic image sensor,[33] (b) spectral photoresponse characteristics of the fabricated organic photoconductive films,[31] and (c) the produced image by test imgae sensor.[33]

via-hole formation with high aspect ratio, as well as issues on the thermal stability and reliability of organic semiconductors. As practical alternative, the hybrid stacked image sensor structures represented in Figure I-5 has been suggested in the representative patents.[35,36] At the bottom, easily separable B-PD and R-PD (or the corresponding two PD such as R-PD and magenta- (Mg)-PD) are vertically or parallely arranged, and G-PD is then added on the top. These stacked structures are supposed to lead to the sensitivity enhancement owing to the increased absorption areas. To optimize stacked image sensors, it is now a priority to develop green-selective OPD with a high efficiency. To date, for green-sensitive OPDs, the composition of ketocyanine-cored chromophore and PCBM has been tested, for which the EQE of 15 % at 525nm at an applied bias of -1 V was obtained.[37] The narrow full width at half maximum (FWHM) of 80 nm was induced by the combined effect of narrow-absorbing chromophore and optical cavity tailoring.

I.2. Electrical properties in OPDs for image sensors

Photodetectors based on organic semiconductors have been suggested to produce low-cost, light-weight, and high efficiency devices. The evaluation of basic parameters is essential for the proper characterization of efficient photoetectors, such as the electrical parameters, that are now briefly reviewed.

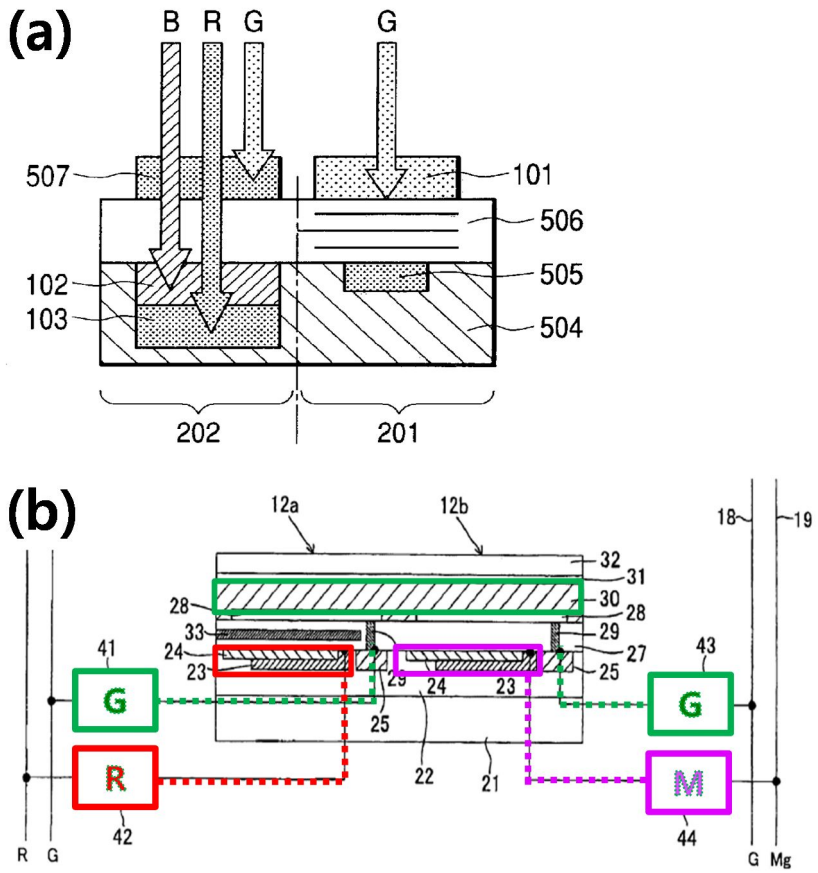

Figure I-5. The schematic vertical views with the configuration of a pixel area of the light-receiving device in the proposed hybrid stacked image sensors. (a) The G-photodetector (PD) on Si-substrate with B-PD and R-PD arranged vertically,[35] and (b) the G-PD on the R-PD and Mg-Pd composed parallelly.[36]

I.2.1. Organic photodetector devices[6,23]

Two different types of photodetection are differentiated: photoconductor and photodiode.

In photoconductors, as shown in Figure I-6a, one carrier may circulate under an applied electric field, while the other carrier is deeply trapped. If the flowing carrier lifetime is long enough, carriers originated at one electrode may reach the other electode, which is at ohmic contact. Because of ohmic contact, more carriers than absorbed photons might flow, with the possible consequence of an efficiency higher than 100 %. However, currents in dark state would be easily flowed, which might be a source of noise in terms of a sensor.

Photodiodes consisting of a donor and an acceptor are comprised between the anode and cathode at different work functions, producing a built-in potential, in Figure I-6b. The photogenerated electrons and holes are separated to the opposite directions by an internal field in the semiconductor junction depletion region. In the simple case of a fully depleted device, high internal quantum efficiency is achieved if $t_{life} > t_{extract}$, where t_{life} is the lifetime of excess charge carriers, and $t_{extract} = L^2/\mu V_{bi}$ is the time taken to transport them to their respective contacts through the built-in field (L is the contact separation, μ is the mobility of the slower carrier and V_{bi} is the built-in potential across the junction). Photodiodes are used in conventional photovoltaic cells or photodetecting sensors requiring low noise.

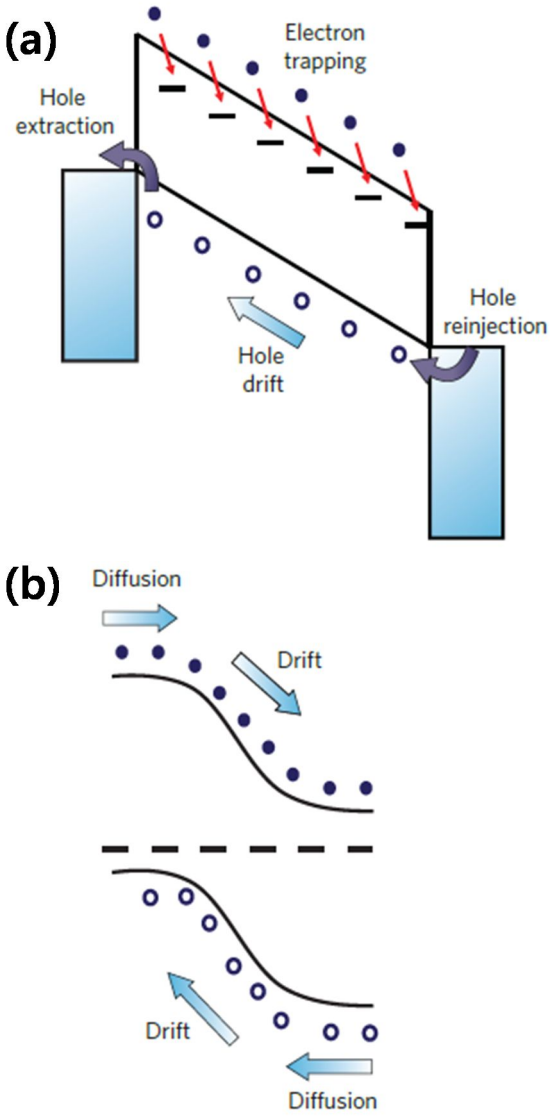

Figure I-6. Charge-separation mechanism of photoconductors and photodiodes. (a) One type of carrier circulates under the influence of an electric field while the other is trapped in a photoconductor. (In this depiction, holes flow but electrons are trapped.) (b) Drift and diffusion of both electrons and holes in a photodiode.[23]

I.2.2. External quantum efficiency[5,6]

For a photodiode device based on exciton dissociation by charge transfer at a donor/acceptor (D/A) interface, η_{EQE} is expressed as the sequential steps;[38]

$$\eta_{EQE} = \eta_A \cdot \eta_{ED} \cdot \eta_{CG} \cdot \eta_{CC} \quad (eq.\ 1)$$

where, η_A is photon absorption leading to the generation of an exciton, η_{ED} is diffusion of the exciton to the D/A interface, η_{CT} is excition dissociation by charge transport (CT) at a D/A interface, and η_{CC} is charge collection of the free charge carriers at the electrodes. The above sequential process is depicted in Figure I-7.[5]

Absorption (η_A): Light absorption is the intial step to transform a photon to a signal carrier under illumination. Silicon has a maximum absorption coefficient around 9.4×10^4 cm^{-1} within the visible range.[39] Many π-conjugated organic semiconductors have superior absorption coefficients, over 1×10^5 cm^{-1}, at that specific wavelength region. However, their relative low mobilities as compared with inorganic semiconductors require the use of thin active layer around 100 nm or below. Therefore, for high EQE, a balance should be considered between light absorption and thickness of the active materials. Additionally, the EQE spectrum of a device is dependent on the absorption spectra of the active D/A materials. Hence, for applications, active materials with moderate absorption spectra should be selected.

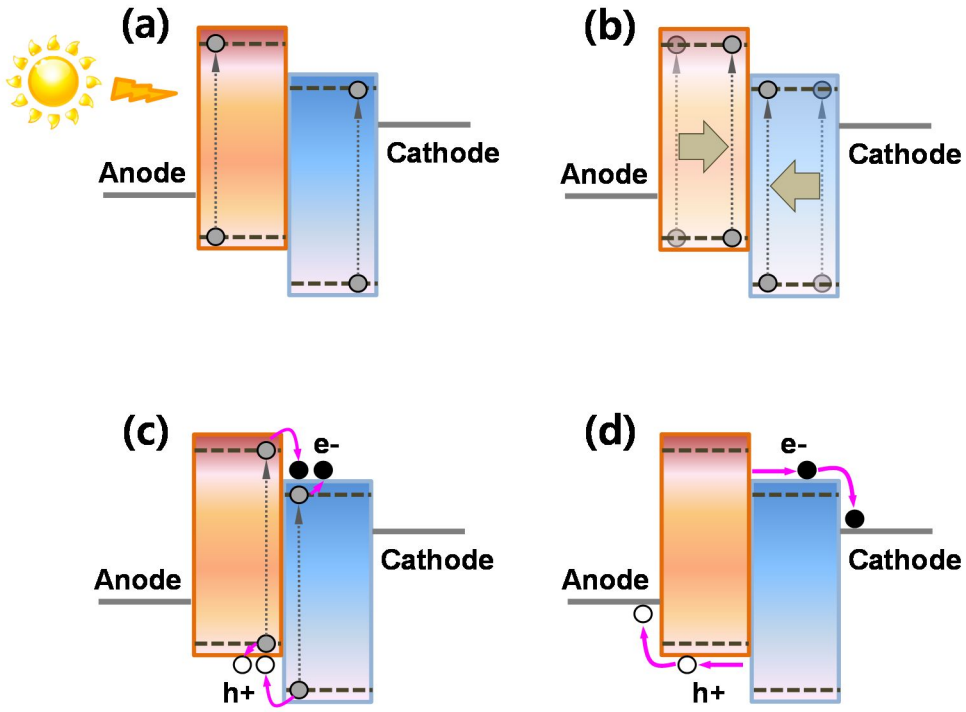

Figure I-7. The conversion process of incident light to electric current in the D/A system with same absorption spectra: (a) photoexcitation and exciton formation, (b) exciton diffusion, (c) exciton dissociation, (d) charge transfer and collection.[5]

Exciton diffusion (η_{ED}): After photons absorption, electron-hole pair excitons are generated at energy higher than the band-gap of organic semiconductors. The photo-generated excitons move to the donor/acceptor interface, where they are dissociated. The diffusion length (L) of excitons is given by the equation $L = (D\tau)^{1/2}$, where D is the diffusion coefficient and τ is the lifetime of the excitons.[5] Considering an exciton lifetime, the diffusion distance is limited to 5 ~ 14 nm,[40] which is significantly less than the photon-absorbed length of about 100 nm. Therefore, the efficiency of devices is limited by the effective exciton diffusion range to the nearest interfaces. The exciton diffusion path depends on the types of heterojunction, either planar heterojunction prepared by layer-by-layer deposition or bulk heterojunction prepared by mixing the donor and the acceptor. The detailed description of the two architectures is as follows:

Planar heterojunction (PHJ): Typically the exciton diffusion length (L_D ~ 5 nm) is known to be shorter than the optical absorption length (L_A ~ 50 – 100 nm). Therefore η_{ED} is often the limiting factor in the bi-layer devices. However, some semiconductors that become crystalline by self-aggregation might maintain the mobility in PHJ, which is favorable in terms of charge transport efficiency.

Bulk heterojunction (BHJ): The BHJ layer structure is obtained by blending or co-depositing D/A molecules, and the diffusion distance of photo-generated

excitons is therefore dependent on the composition ratio that controls the total interface area, regardless of the layer thickness. For this architecture, as the exciton diffusion length of most common organic semiconductors is longer than the transport distance of excitons to interfaces, η_{ED} might ultimately reach 100%.[41] However, the hole and electron after exciton dissociation might easily recombine during transport to the respective electrodes. In photodiode devices, an external field applied for sensing of tiny signals might reduce the e-/h+ recombination, so the charge dissociation efficiency can also be regarded as unity.

Exciton dissociation and charge generation (η_{CG}): At the donor/acceptor interface, excitons might dissociate into free charge carriers. The detailed dissociation process, still unclear, is usally described by two distinct theories.[5] The first theory states that the dissociation occurs in a two-stage process, as the built-in potential between the anode and cathode is too weak to directly dissociate the excitons into free charge carriers. The exciton first reaches the interface and is transformed to a geminate pair (D+/A-) driven by the built-in potential, which corresponds to relative difference between the HOMO of donor and the LUMO of acceptor. Then, the geminate pair dissociates into free charge carriers or recombines to the ground state under external forces such as an applied electric field, thermal energy, *etc*. The second theory stipulates that the built-in field is strong enough to dissociate the exciton

directly into free charge carriers. It is believed that a minimum energy difference of 0.3 eV is required for exciton splitting and charge dissociation.[42]

Charge transport and collection (η_{CC}): For achieving high external quantum efficiency, free electrons and holes should be smoothly transported through the active and transporting layers and collected at the electrode. Therefore, high hole and electron mobilities are critical conditions. The parameters to be optimized to achieve high EQE are different between fullerenes and non-fullerene, when selected as acceptors. In fullerene systems, acceptor-rich compositions are usually preferred for high EQE because of the high electron mobility of fullerene, in comparion to the hole mobility of the donor.[43,44] In contrast, for non-fullerene systems, the best performances were obtained at compositions ensuring a balanced mobilities.[45]

I.2.3. Dark current, responsivity and detectivity

In a simple OPD, the active layer with low conductivity plays the role of a load resistor, which might induce a potential difference between both electrodes. This potential difference generates a current acting in the opposite direction to the photocurrent, whose reverse currents is referred to the dark current $I_{dark}(V)$. For an ideal diode, the dark current density $J_{dark}(V)$ is as follows;[46]

$$J_{dark}(V) = J_0 (e^{qV/k_BT} - 1) \qquad \text{(eq. 2)}$$

where, J_o is a constant, q is the absolute value of electron charge (1.6×10^{-19} Coulombs), k_B is Boltzmann's constant and T is temperature with degree of Kelvin. In BHJ, J_o is dependent on the energy difference bweteen the HOMO of the donor and the LUMO of the acceptor.[47] Dark current is compositively affected by two main factors; one is an active layer morphology based on the molecular structure, composition and processing,[14] the other is injection from the metal contact under an applied external bias voltage.[48] In materials system with self-aggregated property by solution processing, the annealing treatment over the phase transition temperature (T_θ) may change the active layer morphology, which induces to minimize charge injection from a hole transporting layer.[14] The counter-charge injection at the external reverse bias is also caused by shallow energy barrier, hence insertion of a suitable blocking layer (EB) is effective to reduce the dark current with a few nA/cm^2.[48]

For the criterion of light sensitivity, the photoresponsivity (R) is defined as follows;[47]

$$R = \frac{J_{Ph}}{L_{Light}} = \frac{\mathrm{EQE}}{h\nu} \qquad (\mathrm{eq.}\,3)$$

where, J_{Ph} is current density under illumination and L_{Light} is light intensity at the specific wavelength (nm). R is obtained by dividing the EQE by the incident photon energy ($h\nu$) in electron volts (eV).

As the critical parameter considering both photo-sensitivity and dark current of photodiodes, the normalized detectivity (D^*) is expressed as;[47]

$$D^* = \frac{R}{(2qJ_d)^{1/2}} = \frac{J_{ph}/L_{light}}{(2qJ_d)^{1/2}} \quad \text{(eq. 4)}$$

The unit is used as cm $Hz^{1/2}$/W or jones.

High photosesitivity is inevitably accompanied with high dark current due to the same amplification with the photocurrent gain.[49] Therefore, the high detectivity using organic semicondcuctors with high absorption coefficient could be achieved by reducing dark current to the value over 10^{12} cm $Hz^{1/2}$/W, equivalent with the vlaue of inorganic PD such as Si or InGaAs.[10,47,48]

I.2.4. Frequency response

A high frequency photo-response is a critical factor for the performance of electro-optical devices, including sensors. In contrast to inorganic PDs, the frequency response of organic PDs has been poorly investigated. In this section, the required criteria for a high frequency response, as well as a few preliminary works on the measurement methods in particular, are summarized.

As the time-modulated response by exposure of incident light, the -3 dB cut-off frequency (f_c) is defined as the frequency at the decreased photocurrent pulse heigh by a factor of $1/\sqrt{2}$, namely -3 dB.[50] It is reversely proprotional to $2\pi t$ with overall time constant (t) as the root-sum-square value of transit time (t_{tr}) and RC delay time (t_{rc}). The transit time reaching to electrodes of photo-genertated carriers is given by

$t_{tr} = d^2/\mu V$, where d is the layer thickness, μ is a carrier mobility, and V is a voltage drop. The t_{rc} is directly related to the resistance and capacitance (RC). Therefore, the frequency response depends on the carrier mobility and the dielectric constant of organic semiconductors.

Excellent frequency responses using organic semiconductors have been reported, from 430 MHz[51] to 70 MHz[52], for devices fabricated by organic molecular-beam deposition (OMBD) at ultra-high vacuum. For mixed layer structures prepared by the solution process, for instance OPDs composed of P3HT:PCBM, *f*c values between 300 kHz and 1 MHz were reported.[53-55] For conventional thermally-evaporated OPD using the fullerene as acceptor, a high frequency response of 80 MHz was obtained thanks to the high hole mobility of 2.8×10^{-4} cm^2/Vs. It was noted that an increase in mobility by an order of magnitude can lead to a 30-fold increase in the frequency response.[56]

As a useful tool for dynamic characterization, impedance spectroscopy has been recently applied to analyze the frequency response and electrical properties of the material layers and interfaces in OPDs.[57] Basically, the frequency response can be deduced from the resistance and capacitance parameters obtained from the fitted impedance values to the equivalent circuit.[55- 56,58] Recently, electrical parameters such as carrier mobility and lifetime, electron density-of-state, and degradation of OLED device have been investigated.[59-62]

I.3. Organic small molecules for green-sensitive OPD

To realize color-selective organic photodiodes, it is necessary to choose donor and acceptor materials with narrow absorption band widths, and small molecules are therefore preferred to polymers. In general, it is known that p-type materials plays the role of light absorption, generation of exciton, and hole transport from p-n junction to anode.[38] Hence, various organic materials have been investigated as electron donor. In contrast, fullerene derivatives have been almost exclusively used as high performing acceptors in OPV or OPD owing to its favorable LUMO energy, excellent electron transport properties and efficient charge separation because of its 3-dimensional structure.[63] Fullerene derivatives tend to have a broad absorption in the visible range, which is not optimal for the color image sensor applications. Recently, new acceptor materials with efficient charge transport properties in the crystalline state have been suggested as substitutes to fullerene.[64-66] For the purpose of this research, small-molecule organic p-tye and n-type semiconductors with high absorption coefficients between 500 nm and 600 nm are chosen. Existing materials fulfilling this criterion are reviwed below.

I.3.1. Quinacridone

Quinacridone (QA) is industrially known as red colorants. It has a pale yellow in

solution, which changes to vivid red in the solid state due to the intermolecular interactions. The final solid-state color depends on the crystalline phase, for instance, reddish violet in the β-phase and red in the γ-phase.[67]

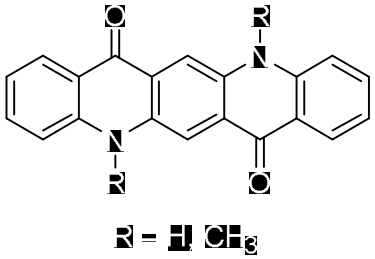

Figure I-8. The molecular structure of quinacridones.

The intermolecular interactions of QA are induced by NH•••O hydrogen bonding between the amine and the carbonyl groups, which also ensure the polymer-like stability in the thin film.[68] This strong hydrogen bonding within QA molecules can change to relatively weak van der Waals interaction by alkyl-substitution, resulting in the shifting of the film absorption spectrum. In the three representative QA compounds, unsubstituted γ-QA with two NH groups, mono-*N*-methylquinacridone (MMQA) with one NH and one CH_3, and *N,N'*-dimethylquinacridone (DMQA) with two CH_3 groups, the maximum absorption positions (λ_{max}) is hypsochromically shifted from γ-QA to MMQA and then DMQA. DMQA exhibits green-absorption with λ_{max} positioned around 540 nm in the thin film state due to less hydrogen bonding.

In addition, QAs have a long fluorescence lifetime of approximately 11 ns in the thin film form, providing enhanced exciton collection yield in bulk heterojunction (BHJ) for OPV devices.[69] It is to be noted that compounds with a high photoluminescent efficiency in solution and a good electrochemical stability in solid state have been suggested as promising candidates for OLED.[70]

I.3.2. Dicyanovinyl thiophene

Dicyanovinyl oligothiophene (DCVnT) is composed of a linear conjugated oligothiophene backbone with a donating character terminated at both extremities with strong electron withdrawing dicyanovinylene groups. The number of thiophene rings can be modulated to easily tune the energy band diagrams as well as the positon of λ_{max} in the absorption spectrum.

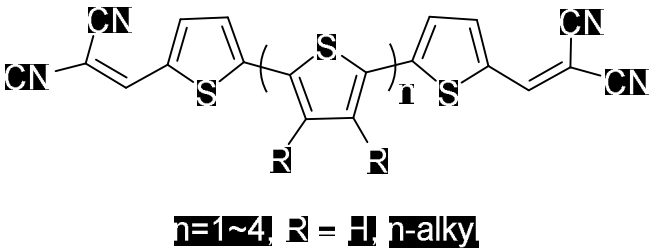

Figure I-9. The molecular structure of dicyanovinyl oligothiophene.

Considering the energy levels, DCV2T and DCV3T show n-type characters, while for a

higher number of thiophene, the HOMO is high enough for efficienct charge dissociation in BHJ with fullerenes as an acceptor.[71] For processing by vacuum deposition, a number of thiophene between 3 and 6 is proper. The optoelectronic properties of DCVnT can also be changed by controlling the position and the length of alkyl side chains. By increasing the number of butyl side chains, the absorption spectrum becomes red-shifted with a narrower band width.[72] However, long alkyl chains might impede the close stacking of neighboring molecules, which might reduce the carrier mobilty because of inefficient hopping transport.[73] Therefore, the alkyl chain length and the position should be chosen also by considering aspects related to the film morphology.

As acceptor in green-selective OPDs, dicyanovinyl-substituted terthiophene with two butyl groups (DCV3T) is an interesting candidate because of its strong absorption in the wavelength range of 500 to 600 nm.

I.3.3. Subphthalocyanine

Boron subphthalocyanine (BSubPc or SubPc), composed of three diiminoisoindole rings *N*-fused around a tetracoordinated boron atom core, is well known as a promising candidate for applications as OPVs as well as OLEDs.[74,75] The symmetrical 14 π-electron aromatic structure both absorbs and emits radiation in the visible spectrum, known as the Q-band between 560 – 600 nm, corresponding to an optical band gap of

2.1 – 2.2 eV. The high symmetry of SubPc also contributes to a large molar extinction coefficient (ε).[76]

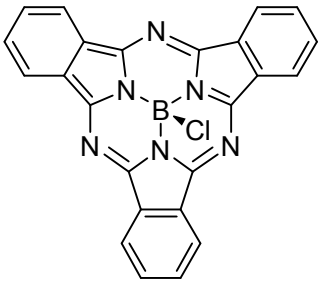

Figure I-10. The molecular structure of boron subphthalocyanine chloride.

The high absorption coefficient and the large band-gap explain the use of SubPc as donor material in OPV with the advantage of a high open-circuit voltage (V_{OC}).[43,77] Its potential as acceptor, as a substitute to fullerene, was also demonstrated in BHJ OPV device by using tetracene as donor.[78] As acceptor, for deeper energy levels, SubPc can be further modified by halogenation or perfluorination at the peripheral positions or in the axial core, at the cost of a narrower absorption band-width and scanty charge dissociation, that induced a low short circuit current (J_{SC}) severely limiting the device performances.[79,80]

To widen the absorption and enhance J_{SC} , it has been recently suggested to choose a

dimer molecular structure[21] or a tri-layer architecture using boron subnaphthalocyanine chloride (SubNc)[81] with red-shifted absorption compared with SubPc.

For green-selective OPDs, the narrow absorption is however not a disadvantage and SubPc is thus a potential acceptor with a high absorption coefficient, that should be combined with a donor that guaranties efficient charge dissociation.

1.4. Research objectives

The wavelength tuning of light absorption or photoluminescence through the modification of the molecular structure of organic semiconductors is commonly handled in the field of organic opto-electronics. In terms of absorption, this approach has been however mostly used for the development of OPV with broad-band absorption and small E_g, in the visible region particularly. High performing color-sensitive PDs could be rapidly commercialized as image sensors, if absorption could be selectively tuned to the green region of the light spectrum. The reason is that in conventional image sensors, the green photodetection surface occupies a double area compared with the blue- or red- photodection surface.[3] The research on green-absorbing organic semiconductors is thus a priority in this field.

In this regard, through the suggestion of potential organic green-absorber candidates and the explanation of their opto-electronic physical behavior in a device, this dissertation is expected to bring an original and significant contribution to the field of image sensor.

The main core of the thesis manuscript is divided into three chapters:

CHAPTER II. Green-Sensitive Organic Photodetector for High Performance Comprising a Bulk Heterojunction of Dimethyl Quinacridone and Dicyanovinyl Terthiophene.

CHAPTER III. High Sensitivity and Spectral selectivity in Green-sensitive Organic Photodetectors Using Subphthalocyanine Derivatives.

CHAPTER IV. Dynamic Characterization of Frequency Response Based on the Molecular Structure.

I.5. Bibliography

1. Martino, N.; Ghezzi, D.; Benfenati, F.; Lanzani, G.; Antognazza, M. R. *J. Mater. Chem. B* **2013**, *1*, 3768-3780.

2. Konstantatos, G.; Clifford, J.; Levina, L.; Sargent, E. H. *Nature Photonics* **2007**, *1*, 531-534.

3. El Gamal, A.; Eltoukhy, H. *IEEE Circuits & Devices Mag.*, **2005**, *21*, 6-20.

4. Clark, J.; Lanzani, G. *Nature Photonics* **2010**, *4*, 438-446.

5. Dong, H.; Zhu, H.; Meng, Q.; Gong, X.; Hu, W. *Chem. Soc. Rev.* **2012**, *41*, 1754-1808.

6. Baeg, K. –J.; Binda, M.; Natali, D.; Caironi, M.; Noh, Y. –Y. *Adv. Mater.* **2013**, *25*, 4267-4295.

7. Zhang, G.; Li, W.; Chu, B.; Su, Z.; Yang, D.; Yan, F.; Chen, Y.; Zhang, D.; Han, L.; Wanga, J.; Liu, H.; Che, G.; Zhang, Z.; Hu, Z. *Org. Elec.* **2009**, *10*, 352-356.

8. Su, Z.; Li, W.; Chu, B.; Li, T.; Zhu, J.; Zhang, G.; Yan, F.; Li, X.; Chen, Y.; Lee, C. -S. *Appl. Phys. Lett.* **2008**, *93*, 103309.

9. Wang, J. B.; Li, W. L.; Chu, B.; Chen, L. L.; Zhang, G.; Su, Z. S.; Chen, Y. R.; Yang, D. F.; Zhu, J. Z.; Wua, S. H.; Yan F.; Liu, H. H.; Lee C. S. *Org. Elec.* **2010**, *11*, 1301-1306.

10. Wu, S. -h.; Li, W. -l.; Chu, B.; Lee, C. -S.; Su, Z. -s.; Wang, J. -h.; Ren, Q. -j. Hu, Z. -z.; Zhang, Z. -q. *Appl. Phys. Lett.* **2010**, *97*, 023306.

11. Li, H. -g.; Wu, G.; Chen, H. -Z.; Wang, M. *Org. Elec.* **2011**, *12*, 70-77.

12. Ng, T. N.; Wong, W. S.; Chabinyc, M. L.; Sambandan, S.; Street, R. A. *Appl. Phys. Lett.* **2008**, *92*, 213303.

13. Van Duren, J. K. J.; Yang, X.; Loos, J.; Bulle-Lieuwma, C. W. T.; Sieval, A. B.; Hummelen, J. C.; Janssen, R. A. J. *Adv. Funct. Mater.* **2004**, *14*, 425-434.

14. Keivanidis, P. E.; Ho, P. K. H.; Friend, R. H.; Greenham, N. C. *Adv. Funct. Mater.* **2010**, *20*, 3895-3903.

15. Keivanidis, P. E.; Khong, S. H.; Ho, P. K. H.; Greenham, N. C.; Friend, R. H. *Appl. Phys. Lett.* **2009**, *94*, 173303.

16. Nalwa , K. S.; Cai, Y.; Thoeming, A. L.; Shinar, J.; Shinar, R.; Chaudhary S. *Adv. Mater.* **2010**, *22*, 4157-4161.

17. Tedde, S. F.; Kern, J.; Sterzl, T.; Furst, J.; Lugli, P.; Hayden, O. *Nano Lett.* **2009**, *9*, 980-983.

18. Baierl, D.; Pancheri, L.; Schmidt, M.; Stoppa, D.; Betta, G. –F. D.; Scarpa, G.; Lugli, P. *Nature Comm.* **2012**, *3*, 1175.

19. Binda, M.; Agostinelli, T.; Caironi, M.; Natali, D.; Sampietro, M.; Beverina, L.; Ruffo, R.; Silvestri, F. *Org. Electon.* **2009**, *10*, 1314-1319.

20. Zimmerman, J. D.; Diev, V. V.; Hanson K.; Lunt, R. R.; Yu, E. K.; Thompson, M. E.; Forrest, S. R. *Adv. Mater.* **2010**, *22*, 2780-2783.

21. Verreet, B.; Rand, B. P.; Cheyns, D.; Hadipour, A.; Aernouts, T.; Heremans, P.; Medina, A.; Claessens, C. G.; Torres, T. *Adv. Energy Mater.* **2011**, *1*, 565-568.

22. Rauch, T.; Boberl, M.; Tedde, S. F.; Furst, J.; Kovalenko, M. V.; Hesser, G.; Lemmer, U.; Heiss, W.; Hayden, O. *Nature Photonics* **2009**, *3*, 332-336.

23. Konstantatos, G.; Sargent, E. H. *Nat. Nanotech.* **2010**, *5*, 391-400.

24. Ghezzi, D.; Antognazza, M. R.; Dal Maschio1, M.; Lanzarini, E.; Benfenati, F.; Lanzani, G. *Nat. Commun.* **2011**, *2*, 166.

25. Gautam, V.; Bag, M.; Narayan, K. S. *J. Am. Chem. Soc.* **2011**, *133*, 17942-17949.

26. Antognazza, M. R.; Scherf, U.; Monti, P.; Lanzani, G. *Appl. Phys. Lett.* **2007**, *90*, 163509.

27. Yu, G. *US 6,300,612* Oct. 9, **2001**.

28. Seo, H.; Aihara, S.; Watabe, T.; Ohtake, H.; Kubota, M.; Egami, N. *Jap. J. Appl. Phys.* **2007**, *46*, L1240-L1242.

29. Aihara, S.; Seo, H.; Namba, M.; Watabe, T.; Ohtake, H.; Kubota, M.; Egami, N.; Hiramatsu, T.; Matsuda, T.; Furuta, M. *IEEE Trans. on Elec. Dev.* **2009**, *56*, 2570-2576.

30. Seo, H.; Aihara, S.; Kubota, M.; Egami, N. *Jap. J. Appl. Phys.* **2010**, *49*, 111601.

31. Seo, H.; Aihara, S.; Watabe, T.; Ohtake, H.; Sakai, T.; Kubota, M.; Egami, N.; Hiramatsu, T.; Matsuda, T.; Furuta, M.; Hirao, T. *Jap. J. Appl. Phys.* **2011**, *50*, 024103.

32. Sakai, T.; Seo, H.; Aihara, S.; Kubota, M.; Egami, N.; Wang, D.; Furuta, M. *Jap. J. Appl. Phys.* **2012**, *51*, 010202.

33. Sakai, T.; Seo, H.; Aihara, S.; Kubota, M.; Furuta, M. *Proc. SPIE* **2013**, *8659*, 86590G-1~8.

34. Higashi, Y.; Kim, K.-S.; Jeon, H.-G.; Ichikawa, M. *J. Appl. Phys.* **2010**, *108*, 034502.

35. Iwasaki, T. *US 7,129,466* Oct. 31, **2006**.

36. Goto, T.; Suzuki, N. *US 7,667,750* Feb. 23, **2010**.

37. Lyons, D. M.; Armin, A.; Stolterfoht, M.; Nagiri, R. C.R.; Jansen-van Vuuren, R. D.; Pal, B. N.; Burn, P. L.; Lo, S. -C.; Meredith, P. *Org. Electron.* **2014**, *15*, 2903-2911.

38. Peumans, P.; Yakimov, A.; Forrest, S. R. *J. Appl. Phys.* **2003**, *93*, 3693-3723.

39. Green, M. A. *Solar Energy Mater. & Solar Cells* **2008**, *92*, 1305-1310.

40. Markov, D. E.; Amsterdam, E.; Blom, P. W. M.; Sieval, A. B.; Hummelen, J. C. *J. Phys. Chem. A* **2005**, *109*, 5266-5274.

41. Pandey, R.; Holmes, R. J. *Appl. Phys. Lett.* **2012**, *100*, 083303.

42. Dennler, G.; Scharber, M. C.; Brabec, C. *Adv. Mater*. **2009**, *21*, 1323−1338.

43. Pandey, R.; Gunawan, A. A.; Mkhoyan, K. A.; Holmes, R. J. *Adv. Funct. Mater.* **2012**, *22*, 617-624.

44. Wei, G.; Wang, S.; Renshaw, K.; Thompson, M. E.; Forrest, S. R. *ACS Nano* **2010**, *4*, 1927-1934.

45. Schwartz, G.; Ke, T. -H.; Wu, C. -C.; Walzer, K.; Leo, K. *Appl. Phys. Lett.* **2008**, *93*, 073304.

46. Nelson, J. *In The Physics of Solr Cells* Imperial College Press: London, **2003**.

47. Gong, X.; Tong, M.; Xia, Y.; Cai, W.; Moon, J. S.; Cao, Y.; Yu, G.; Shieh, C. -L.; Nilsson, B.; Heeger, A. J. *Science* **2009**, *325*, 1665-1667.

48. Binda, M.; Iacchetti, A.; Natali, D.; Beverina, L.; Sassi, M.; Sampietro, M. *Appl. Phys. Lett.* **2011**, *98*, 073303.

49. Ryzhii, V.; Khmyrova, I.; Ryzhii, M.; Mitin, V. *Semicond. Sci. Techonol.* **2004**, *19*, 8-16.

50. Baierl, D.; Fabel, B.; Lugli, P.; Scarpa, G. *Org. Electron.* **2011**, *12*, 1669-1673.

51. Peumans, P.; Bulovic, V.; Forrest, S. R. *Appl. Phys. Lett.* **2000**, *76*, 3855-3857.

52. Morimune, T.; Kajii, H.; Ohmori, Y. *IEEE Photonic. Tech. Lett.* **2006**, *18*, 2662-2664.

53. Punke, M.; Valouch, S.; Kettlitz, S. W.; Christ, N.; Gärtner, C.; Gerken, M.; Lemmer, U. *Appl. Phys. Lett.* **2007**, *91*, 071118.

54. Arredondo, B.; de Dios, C.; Vergaz, R.; Criado, A. R.; Romero, B.; Zimmermann, B.; Würfel, U. *Org. Electron.* **2013**, *14*, 2484-2490.

55. Arredondo, B.; de Dios, C.; Vergaz, R.; del Pozo, G.; Romero, B. *IEEE Photon. Tech. Lett.* **2012**, *24*, 1868-1871.

56. Tsai, W. –W.; Chao, Y. –C.; Chen, E. –C.; Zan, H. –W.; Meng, H. –F.; Hsu, C. –S. *Appl. Phys. Lett.* **2009**, *95*, 213308.

57. Barsoukov, E.; Macdonald, J. R. *In Impedance Spectroscopy Theory, Experiment, and ApplicationsCells* Wiley-Interscience: Hoboken, New Jersey, **2005**.

58. Perrier, G.; de Bettignies, R.; Berson, S.; Lemaıtre, N.; Guillerez, S. *Solar Energy Mater. & Solar Cells* **2012**, *101*, 210-216.

59. Garcia-Belmonte, G.; Munar, A.; Barea, E. M.; Bisquert, J.; Ugarte, I.; Pacios, R. *Org. Electron.* **2008**, *9*, 847-851.

60. Tripathi, D. C.; Tripathi, A. K.; Mohapatra, Y. N. *Appl. Phys. Lett.* **2011**, *98*, 033304.

61. Garcia-Belmonte, G.; Boix, P. P.; Bisquert, J.; Sessolo, M.; Bolink, H. J. *Solar Energy Mater. & Solar Cells* **2010**, *94*, 366-375.

62. Nowy, S.; Ren, W.; Elschner, A.; Lövenich, W.; Brütting, W. *J. Appl. Phys.* **2010**, *107*, 054501.

63. Bendikov, M.; Wudl, F.; Perepichka, D. F. *Chem. Rev.* **2004**, *104*, 4891-4946.

64. Anthony, J. E. *Chem. Mater.* **2011**, *23*, 583-590.

65. Zhan, X.; Facchetti, A.; Barlow, S.; Marks, T. J.; Ratner, M. A.; Wasielewski, M. R.; Marder, S. R. *Adv. Mater.* **2011**, *23*, 268-284.

66. Stolar, M.; Baumgartner, T. *Phys. Chem. Chem. Phys.* **2013**, *15*, 9007-9024.

67. Paulus, E. F.; Leusen, F. J. J.; Schmidt, M. U. *Cyst. Eng. Comm.* **2007**, *9*, 131-143.

68. Mizuguchi, J.; Senju, T. *J. Phys. Chem. B*, **2006**, *11*0, 19154-19161.

69. Chen, J. J.-A.; Chen, T. L.; Kim, B. S.; Poulsen, D. A.; Mynar, J. L.; Fréchet, J. M. J.; Ma, B. *ACS Appl. Mater. Interfaces* **2010**, *2*, 2679-2686.

70. Wang, J.; Zhao, W.; Dou, C.; Sun, H.; Xu, P.; Ye, K.; Zhang, J.; Jiang, S.; Li, F.; Wang, Y. *J. Phys. Chem. B*, **2007**, *111*, 5082-5089.

71. Fitzner, R.; Reinold, E.; Mishra, A.; Mena-Osteritz, E.; Ziehlke, H.; Körner, C.; Leo, K.; Riede, M.; Weil, M.; Tsaryova, O.; Weiß, A.; Uhrich, C.; Pfeiffer, M.; Bäuerle, P. *Adv. Funct. Mater.*, **2011**, *21*, 897-910.

72. Ziehlke, H.; Fitzner, R.; Koerner, C.; Gresser, R.; Reinold, E.; Bäuerle, P.; Leo, K.; Riede, M. K. *J. Phys. Chem. A*, **2011**, *115*, 8437-8446.

73. Schulze, K.; Riede, M.; Brier, E.; Reinold, E.; Bäuerle, P.; Leo, K. *J. Appl. Phys.* **2008**, *104*, 074511.

74. Claessens, C. G.; González-Rodríguez, D.; Torres, T. *Chem. Rev*. **2002**, *102*, 835-853.

75. Morse, E.; Bender, T. P. *ACS Appl. Mater. & Interfaces* **2012**, *4*, 5055-5068.

76. Fulford, M. V.; Jaidka, D.; Paton, A. S.; Morse, G. E.; Brisson, E. R. L.; Lough, A. J.; Bender, T. P. *J. Chem. Eng. Data* **2012**, *57*, 2756-2765.

77. Gommans, H.; Cheyns, D.; Aernouts, T.; Girotto, C.; Poortmans, J.; Heremans, P. *Adv. Funct. Mater.* **2007**, *17*, 2653-2658.

78. Beaumont, N.; Cho, S. W.; Sullivan, P.; Newby, D.; Smith, K. E.; Jones, T. S. *Adv. Funct. Mater.* **2012**, *22*, 561-566.

79. Sullivan, P.; Duraud, A.; Hancox, I.; Beaumont, N.; Mirri, G.; Tucker, J. H. R.; Hatton, R. A.; Shipman, M.; Jones, T. S. *Adv. Funct. Mater.* **2011**, *21*, 352-355.

80. Gommans, H.; Aernouts, T.; Verreet, B.; Heremans, P.; Medina, A.; Claessens, C. G.; Torres, *T. Adv. Funct. Mater.* **2009**, *19*, 3435-3439.

81. Cnops, K.; Rand, B. P.; Cheyns, D.; Verreet, B.; Empl, M. A.; Heremans, P. *Nature Comm.* **2014**, *5*, 3406.

Chapter II.
High Performance Green-Sensitive Organic Photodetector Consisting of the Bulk Heterojunction of Dimethylquinacridone and Dicyanovinyl terthiophene

II.1. Introduction

For application of organic green (G) -sensitive OPD as image sensors, one of the biggest challenges is to find substitutes to fullerene derivatives with high electron mobility, because of their absorption in the blue region of the light spectrum. As alternative acceptor, perylene diimide derivatives have been tested for G-OPD, but the EQE did not exceed 7 % at 3 V with high dark currents.[1] The development of new acceptors with high absorption coefficient in the wavelength range between 500 nm and 600 nm is indispensable for efficient G-OPD.

EQE, which is a central governing parameter of the performance of OPD, can be maximized by optimizing the following sequence including the absorption, exciton diffusion, charge dissociation, and charge collection.[2] In sensors, the dependence of EQE on these parameters can be function of the applied bias voltage, which is usually used to amplify small amplitude signals. Therefore, the analysis of EQE parameters in devices based on the BHJ structure comprising non-fullerene small molecules, under

applied reverse bias voltage, is critical for a further improvement of green photodetectors.

In this study, it is demonstrated the realization of a green-selective OPD with DMQA as the donor and a DCV3T derivative as the acceptor an operating voltage of -5 V. It was investigated the electrical and optical behaviours of OPDs consisting of DMQA and DCV3T BHJ films with different compositions. The absorption coefficient, charge transport, and charge photogeneration efficiency were assessed in detail. Device efficiency was characterized by the maximum efficiency of charge photogeneration at BHJ interfaces with sufficient light absorption, and the balance of electron and hole mobilities. To interpret the device performance in detail, transient absorption spectroscopy (TAS) and the space-charge-limited-current method were used to measure the efficiency of charge photogeneration and the carrier mobilities, respectively.

II.2. Experimental

Materials: N,N-dimethyl quinacridone (DMQA) (Lumtec, > 99% purity) and dicyanovinyl terthiophene (DCV3T) (> 99% purity) were used as the donor and acceptor materials, respectively. Molybdenum oxide (MoO_x) was purchased from Sigma Aldrich Chemical Co without further purification.

Device fabrication: Organic photodiodes were fabricated on glass substrates pre-

coated with indium-tin-oxide (ITO) with a sheet resistance of 15 Ω per square. The organic layers and Al cathode were deposited using vacuum thermal evaporation at a base pressure $<2 \times 10^{-7}$ Torr. All organic layers were deposited at a total rate of 0.1 nm/s. A 30 nm thick layer of MoOx was also deposited using vacuum thermal evaporation with the deposition rate of 0.1 Å/s. The Al cathode was deposited at a rate of 0.2 nm/s through a shadow mask with an active area of 0.04 cm^2. The hole-only devices were fabricated by depositing layers consisting of 30 nm MoO_x, 70 nm BHJ, 30 nm MoO_x, and 80 nm Al metal onto the ITO. The electron-only devices were prepared by sequentially depositing a 30 nm pristine DCV3T film, a 70 nm BHJ layer, and a 80 nm Al layer onto the ITO. After device formation, glass encapsulation was performed using UV exposure for 5 min.

Device characterization: Current–voltage (*J–V*) characteristics were measured using a Keithley K4200 semiconductor parameter analyzer, and the light response was measured under illumination from a white LED with a broad range of emission wavelengths of 400 to 675 nm and light output intensity of approximately 5 mW/cm^2. The external quantum efficiency (EQE) was measured using a spectral incident photon-to-electron conversion efficiency (IPCE) measurement system under monochromatic light generated by an ozone-free Xe lamp with a chopper frequency of 30 Hz. A calibrated Si-PD was used to measure the incident monochromatic light intensity. The incident light power was measured to be 176 $\mu W/cm^2$ at the wavelength

of 540 nm.

Absorbance and photoluminescence: Absorption spectra of organic films grown on glass substrates were collected using a spectrophotometer (Shimadzu UV-240). The photoluminescence spectra were obtained using a fluorescence spectrometer (Hitachi corp., F7000) equipped with a Xe lamp as the light source.

Transient absorption spectroscopy: Ultrafast transient absorption spectra were collected using a pump-probe system (Ultrafast System, Helios). A pump beam with a pulse energy of 60 nJ at 540 nm was obtained from an optical parametric amplifier (Light conversion, TOPAS-C), pumped by a regeneratively amplified Ti:Sapphire laser system (Coherent, Libra, 800 nm wavelength, 50 fs pulse duration, 1 kHz repetition rate). The probe beam was a white light continuum generated by focusing a small portion of the amplifier output though a sapphire window. All measurements were carried out under ambient conditions.

II.3. Result and discussion

II.3.1. Device performance by ratio modulation in a bulk heterojunction structure

Figure II-1 shows the molecular structures and energy levels of DMQA[3] and DCV3T.[4] The offset of LUMO levels between the two active materials was estimated to be

approximately 0.9 eV, which favors efficient charge separation.[5]

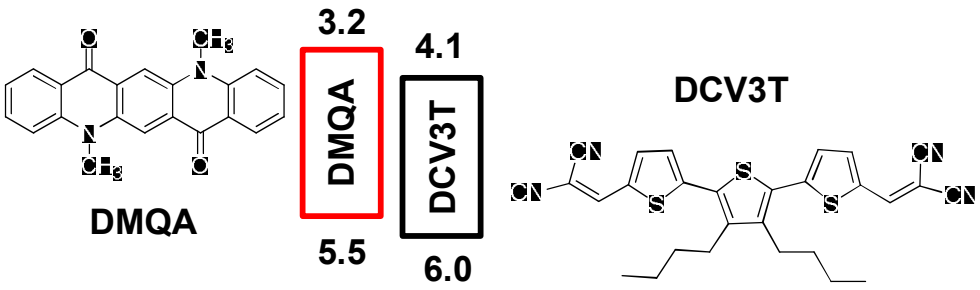

Figure II-1. Molecular structures of N,-N dimethyl quinacridone (DMQA) and dibutyl-substituted dicyanovinyl-terthiophene (DCV3T).

From the absorption spectra shown in Figure II-2a, it can be seen that DMQA exhibited a maximum absorption peak at 538 nm with an absorption coefficient of approximately 4.10×10^4 cm^{-1} and a narrow full-width-at-half-maximum (FWHM) of 92 nm, indicating high green color selectivity. In contrast, DCV3T showed a maximum absorption peak at 534 nm, with a high absorption coefficient of 1.14×10^5 cm^{-1}, which is around three times higher than that of DMQA, but a relatively broad FWHM of 161 nm was found, mainly due to the shoulder peak based on the intermolecular excitonic interaction in the film state.[4] By blending DMQA and DCV3T in a simple 1:1 ratio, an intermediate absorption peak at 530 nm, which is just the arithmetic sum of the absorbances from individual components, to give a high absorption coefficient of

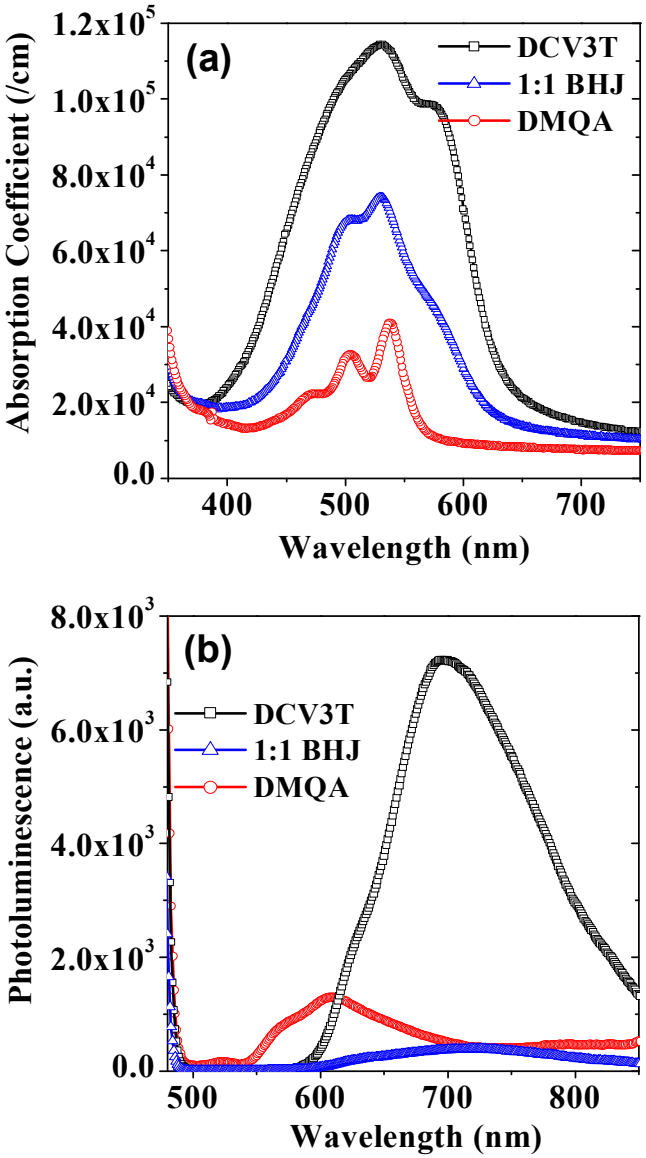

Figure II-2. Optical properties of thin films. (a) UV-Vis absorption spectra, and (b) photo-luminescence spectra of the thin films.

7.4×10^4 cm^{-1} and a FWHM of 130 nm were obtained. These results suggest that this BHJ system is suitable for a green color absorbing organic layer. The photoluminescence (PL) of the corresponding materials was also measured and the results are shown in Figure II-2b. DCV3T produced a PL intensity that was moderately higher than that of DMQA, but was significantly quenched by mixing the two, indicating efficient exciton dissociation in DMQA-DCV3T BHJ film.[6,7]

To investigate the electrical and optical characteristics of the OPDs in detail, devices were prepared with different compositions of DMQA and DCV3T (3:1 (DMQA-rich), 1:1, and 1:3 (DCV3T-rich)). Analysis of the surface morphology of the pure DMQA, pure DCV3T and the blended films are shown in Figure II-3. The pure DMQA and pure DCV3T films showed root-mean-square (rms) roughness of 28.9 ± 1.3 nm and 20.6 ± 0.7 nm, respectively, attributed to the significant self-aggregation based on their intrinsically compact molecular structures.[8,9] In contrast, the active layer roughnesses of the 3:1, 1:1, and 1:3 DMQA/DCV3T films were 1.95 ± 0.48 nm, 0.48 ± 0.11 nm, and 0.41 ± 0.02 nm, respectively, demonstrating smoother morphologies than those of the two neat films.

The structure of the OPDs was simplified in order to examine the effects of ratio modulation in the BHJ layer. Devices were fabricated on ITO-coated glass by sequential deposition of a 30 nm layer of MoOx as an excellent hole extraction layer,[10] a 70 nm BHJ layer of DMQA and DCV3T, and an 80 nm Al electrode. The reverse bias

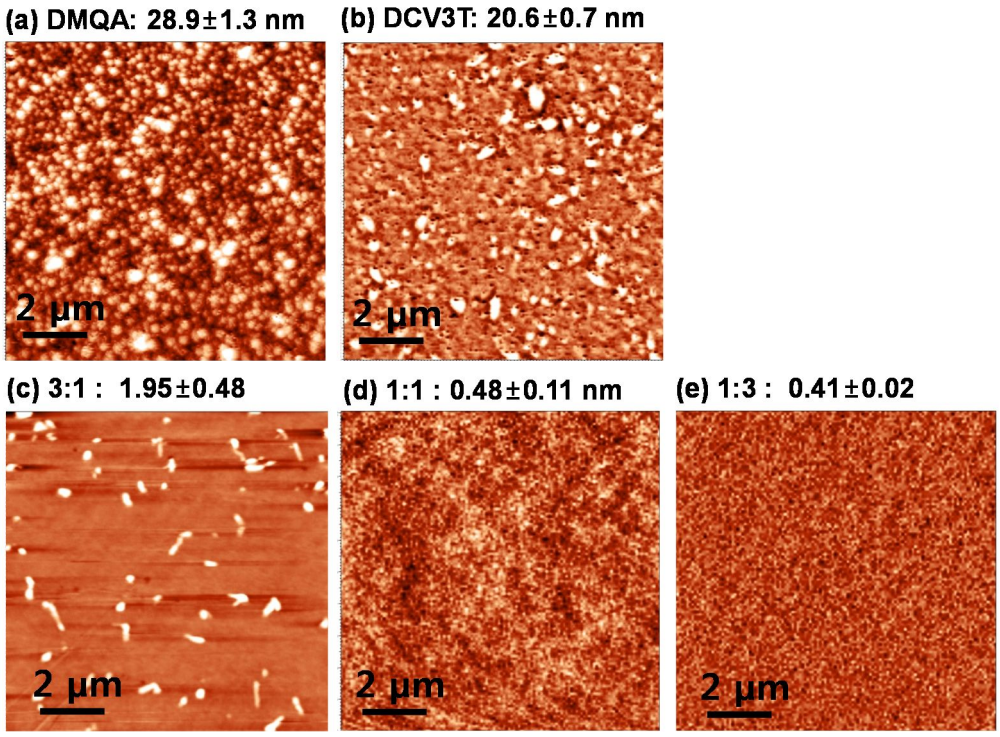

Figure II-3. Atomic force microscopic topography of (a) neat DMQA, (b) neat DCV3T, (c) 3:1 BHJ, (d) 1:1 BHJ, and (e) 1:3 BHJ films. The field area of each film is 10 μm × 10 μm.

was made by applying negative voltage to the ITO electrode. Figures II-4a-c show the EQE spectra of the devices with different compositions of DMQA and DCV3T under different reverse bias. In Figure II-4a, OPDs with compositions of 3:1, 1:1, and 1:3 exhibited zero-biased EQEs of 11.1%, 27.5%, and 15.3%, respectively, at 540 nm. All of the OPDs exhibited a strong bias-dependent enhancement of EQEs.[11] For instance, the EQEs of the devices with 3:1, 1:1, and 1:3 mixing ratios measured at a −3 V reverse bias were 41.8%, 61.7%, and 47.8%, respectively, at a wavelength of 540 nm (Figure II-4b). A further increase in reverse bias up to −5 V resulted in considerably enhanced device efficiency, as shown in Figure II-4c. A maximum EQE of 67.6% at 540 nm with an applied reverse bias voltage of −5 V was obtained from the OPD with the 1:1 BHJ ratio, which is comparable to the EQEs accomplished with polymer-based OPDs (65–75%).[12-14] These results indicate that the 1:1 BHJ ratio of DMQA/DCV3T may be close to the optimum composition for high efficiency green OPDs. The absorption spectra of the BHJ layers with different mixing ratios are further plotted in Figure II-4d.

The BHJ layer with a 1:3 ratio (DCV3T-rich) exhibited a higher absorption coefficient than the other BHJ layers, which is expected because of the higher absorption coefficient of pristine DCV3T compared to that of DMQA (Figure II-2a). It is well known that high absorption intensity of the active layer is regarded as one of the critical parameters for improving the efficiency of OPDs and organic solar cells.[15]

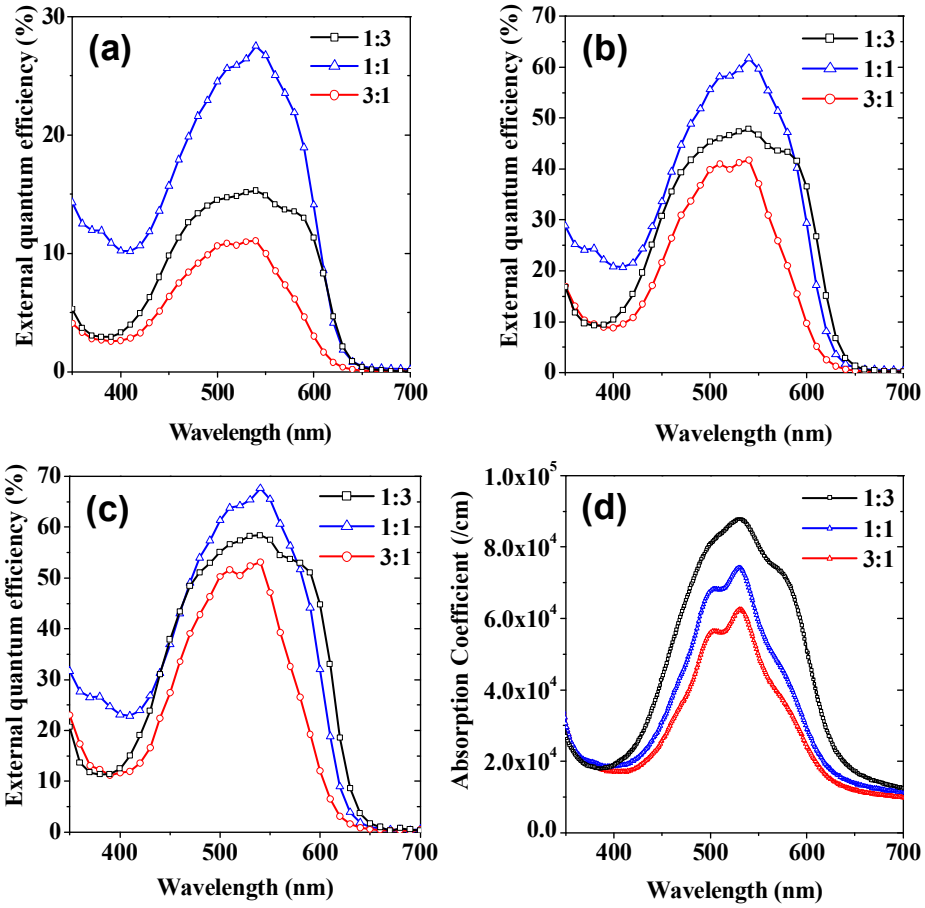

Figure II-4. External quantum efficiency (EQE) spectra for a BHJ OPD with mixed composition ratios of DMQA/DCV3T of 3:1, 1:1, and 1:3 (a) at zero-bias, (b) at an applied voltage of −3 V, and (c) −5 V. (d) The absorption spectra for mixtures of DMQA and DCV3T as a function of composition.

However, OPDs with a BHJ ratio of 1:3 DMQA/DCV3T showed much lower EQEs compared to devices with a 1:1 ratio, suggesting that the presence of an additional mechanism via either charge generation or charge transport may influence the device performance.[2]

The current density–voltage (*J–V*) characteristics of the OPDs with different BHJ component ratios are shown in Figure II-5. All devices exhibited similar reverse dark current densities of around 3×10^{-7} A/cm^2 at a −3 V bias. In contrast, different rectification characteristics were evident in the forward current direction. For instance, the OPD with a 1:1 DMQA/DCV3T ratio produced a typical diode curve with a rectification ratio of 2.21×10^4 at ± 3 V, whereas those of the devices with 1:3 and 3:1 mixing ratios showed reduced values of 8.25×10^2 and 2.60×10^1 at ± 3 V, respectively. This was mainly attributed to the reduction in the forward dark current densities. Similar reductions in the forward current were also observed for the devices under illumination conditions, indicating that the BHJ ratios significantly influence the charge transport in the devices, resulting in variations in device efficiency.[16,17]

The OPD with a BHJ component ratio of 1:1 resulted in the largest photo-response under reverse bias, while the photo-current density rapidly decreased for the 1:3 ratio and was reduced even further for the 3:1 ratio device, which is consistent with the EQE variations shown in Figure II-4.

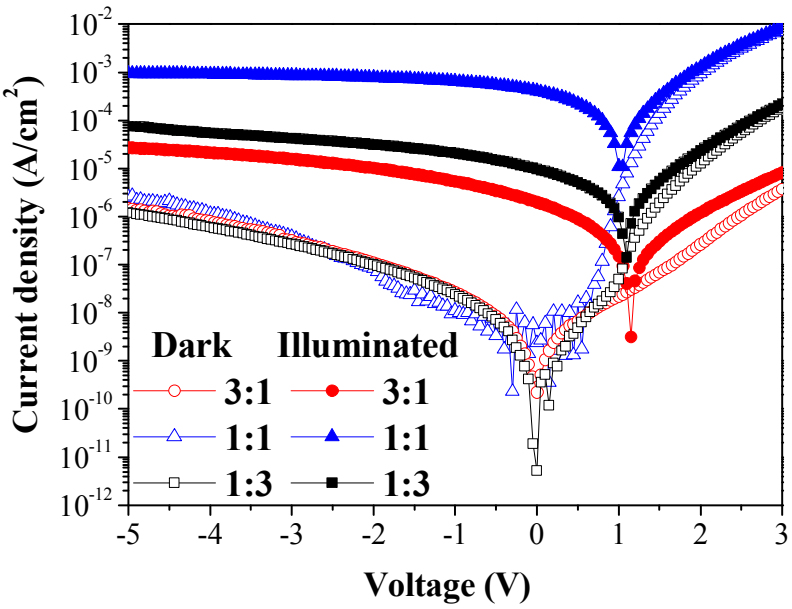

Figure II-5. Current density–voltage characteristics in the dark and under illumination at 5 mW/cm^2 for BHJ devices with composition ratios of DMQA/DCV3T of 3:1, 1:1, and 1:3.

II.3.2. Analysis on charge generation and transport for high performance

The charge transport characteristics of the devices were further investigated by measuring the carrier mobilities. The hole-only devices were fabricated by depositing a 30 nm MoOx film on ITO-coated glass, followed by a 70 nm BHJ layer, another 30 nm MoOx layer, and an 80 nm Al electrode layer. The electron-only devices were prepared by sequentially depositing a 30 nm pristine DCV3T layer on the ITO, followed by a 70 nm BHJ layer, and 80 nm Al. The hole and electron mobilities of the devices were extracted using the conventional space-charge limited current model[16] and the results are summarized in Table II-1. The pristine DMQA had a hole mobility of 1.23×10^{-6} cm^2/Vs at an applied electric field of 0.2 MV/cm, which then decreased with increasing amount of DCV3T in the blended film, reaching 2.40×10^{-9} cm^2/Vs for the 1:3 DMQA /DCV3T.

The film containing solely DCV3T exhibited an electron mobility of 2.46×10^{-6} cm^2/Vs, which then decreased with increasing amount of DMQA, reaching 1.23×10^{-9} cm^2/Vs for the 3:1 DMQA/DCV3T. For the 1:1 ratio, almost identical carrier mobilities of around 2×10^{-8} cm^2/Vs were observed. It should be noted that the 1:1 BHJ ratio resulted in the highest photocurrent density as well as EQE of the device, while both 3:1 and 1:3 ratios exhibiting significantly degraded device performance (see Figures II-4 and

Table II-1. Field-induced carrier mobility derived from mixed DMQA/DCV3T single carrier devices using the space-charge limited current model. (Electric field: 0.2 MV/cm)

Composition ratio	DMQA - only	3:1 (DMQA - rich)	1:1	1:3 (DCV3T - rich)	DCV3T - only
Hole-Mobility (cm^2/V.s)	1.23×10^{-6}	2.11×10^{-7}	2.03×10^{-8}	2.40×10^{-9}	-
Electron-Mobility (cm^2/V.s)	-	1.23×10^{-9}	2.33×10^{-8}	1.73×10^{-7}	2.46×10^{-6}

II-5). These results imply that the higher device efficiency achieved with the mixing ratio of 1:1 may be related to the balance in charge carrier mobility[15,18,19] and the consequent minimization of charge recombination.[16,17,20] However, the charge imbalance observed is similar for the devices with the BHJ ratios of 3:1 and 1:3, but the EQE and the photocurrent density of the 1:3 device are clearly higher than those of the 3:1 device most likely due to the higher absorbance of the former device than that of the latter.

To study the overall efficiency of exciton diffusion and charge transfer at the interfaces, it was performed by ultrafast transient absorption (TA)[21] studies on a series of thin films made from DMQA and DCV3T. An estimate of the relative charge generation efficiency in BHJ films requires interpretation of the spectral signature and relaxation dynamics of DMQA and DCV3T excitons. Figure II-6 shows TA spectra of DMQA, DCV3T, and DMQA/DCV3T 1:1 ratio at several delay times from 0.4 ps to 5 ns. The pump fluence was maintained at 7 μJ/cm^2 to avoid any undesired exciton decay channels such as biexciton annihilation.[22] The spectral signatures in the region of 500–600 nm originate from ground state bleaching (GSB) and those in the region of 650–800 nm are the sum of two contributions from photoinduced absorption (PIA) and stimulated emission (SE), with the former dominating to give overall negative $\Delta T/T$.

At the pump-probe delay of 0.4 picoseconds, the neat DCV3T film in Figure II-6b shows a broad band with high intensities at the GSB and PIA regions. In contrast, the

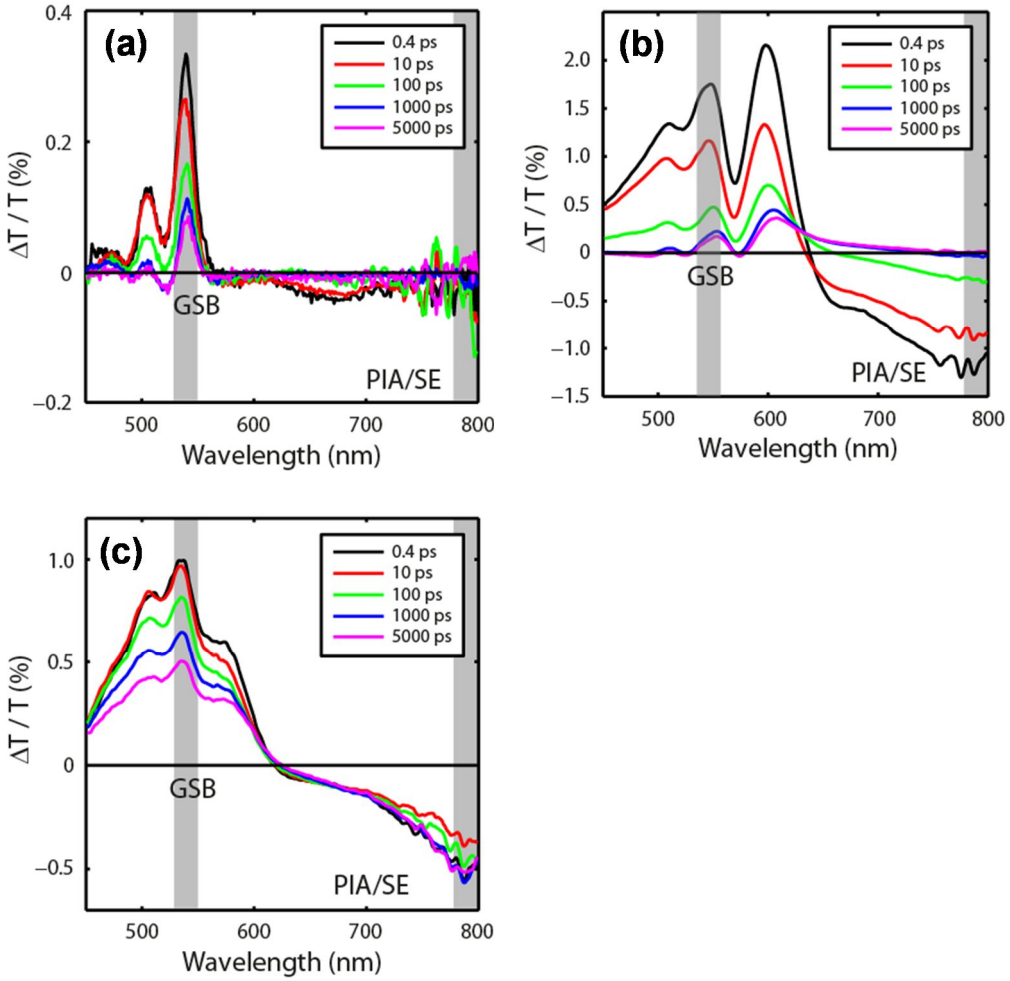

Figure II-6. Transient absorption (TA) spectra of (a) neat DMQA and (b) neat DCV3T films, and (c) BHJ films with a composition ratio of 1:1 at representative pump-probe delay times from 400 fs to 5 ns.

TA spectrum of the neat DMQA film in Figure II-6a exhibit narrow and low absorptions, and there is little PIA signal. The low absorption of DMQA results in low exciton generation. The 1:1 DMQA/DCV3T film shows intermediate intensity in the GSB and PIA regions compared to the neat DCV3T and DMQA films, as shown in Figure II-6c. Interestingly, the neat DCV3T film shows ultrafast signal decay within 100ps, while the signals of BHJ films do not decrease considerably. For the neat films, the DCV3T film shows an initial fast decay within 100ps due to exciton recombination, and the DMQA film shows an already low intensity from the initial time scale. The exciton lifetimes of DCV3T and DMQA are less than 100 ps. In contrast, the PIA decay profiles in the 1:1 BHJ film exhibits high intensities up to 5ns.

TA kinetics for GSB and PIA are expressed as the normalized values by the integration in the ranges of 520–550 nm and 770–800 nm, respectively. The integration range of GSB corresponds to the absorption peak maxima of neat and BHJ films taken from Figure II-2a and that of the PIA kinetics was chosen to include PIA contribution only, avoiding any SE contribution (See Figure II-2b for emission spectra). From the GSB kinetics of two neat films in Figure II-7a, it was found that the 1/e-lifetime of excitons was 38 ps for DCV3T and 146 ps for DMQA. A comparable value of 42 ps was obtained from the PIA kinetics of DCV3T.

The TA kinetics of the BHJ films shown in Figure II-7b are quite different from those of the neat films. The GSB kinetics showed much slower recovery of ground state

population and the PIA kinetics demonstrated increased absorption that was constant over several nanoseconds. The PIA signal of the BHJ films was attributed to free charge carriers generated from exciton dissociation. The PIA signal could not occur from excitons as their lifetime is much shorter. In the 1:1 DMQA/DCV3T film, the PIA signal decayed initially during the first 1–2 ps and then increased up to approximately 500 ps. This indicates that the initial PIA signal originated from excited state absorption by excitons and the remaining part of the PIA signal is mainly due to free charge carriers after exciton dissociation by electron transfer. This effect was clearly seen in the 1:3 film, where DCV3T was the major component. Initially, the PIA signal decayed faster than that of DCV3T due to charge transfer at dissociation sites, and reached a plateau after a few hundred picoseconds, indicating that charge generation was complete. From the analysis of the PIA signals, it could be estimated the efficiency of carrier generation in the BHJ films. Because the PIA kinetics were normalized with respect to the corresponding GSB maximum, the intensity of the PIA signal was directly proportional to the number of charge carriers generated per absorbed photon. Assuming the efficiency of charge generation in the 1:1 film was unity, the carrier generation efficiency of the 3:1 and 1:3 films were calculated to be 0.79 and 0.27, respectively.

The difference in charge generation efficiencies among the three BHJ films may be further explained by the relationship between nanoscopic morphology and exciton

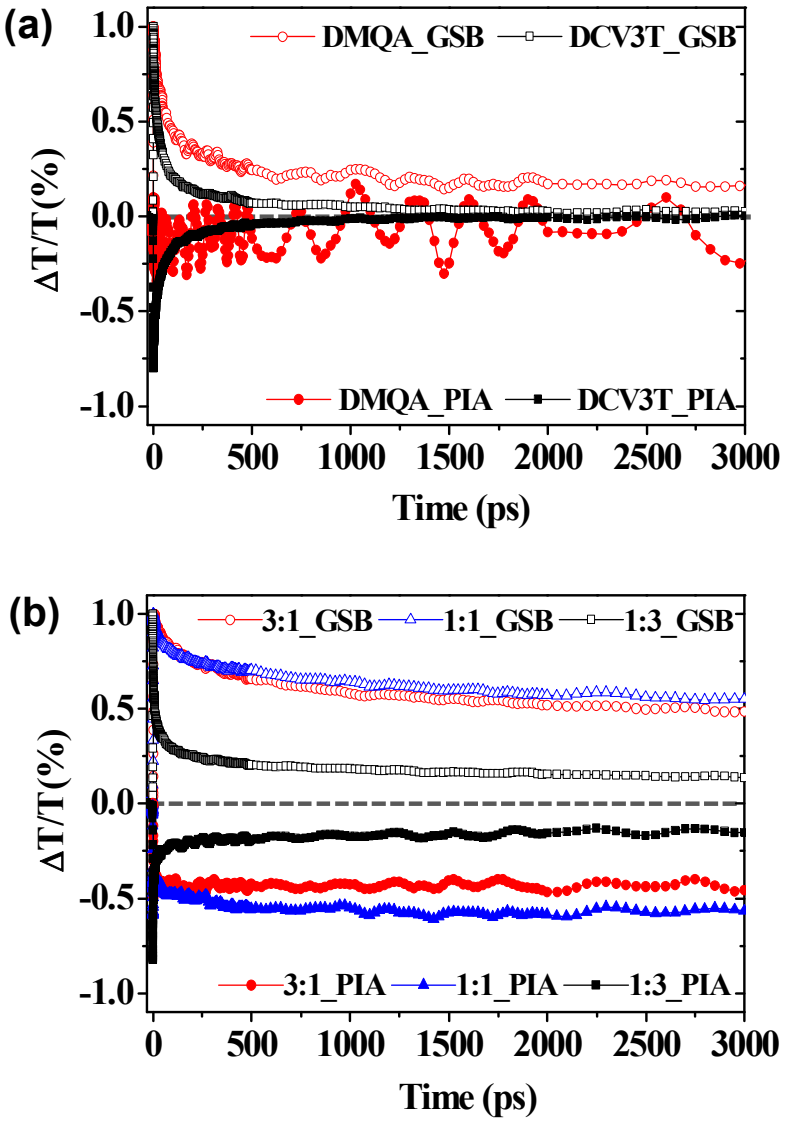

Figure II-7. Normalized TA kinetics (a) of the two neat films, and (b) of the three BHJ films with composition ratios of DMQA/DCV3T of 3:1, 1:1, 1:3.

lifetime. From AFM measurements carried out on the BHJ films (Figure II-3), it can be inferred that all three films have well dispersed p- and n-domains, with no phase separation evident in the images. However, nanoscale surface morphology that cannot be probed by AFM because of the small feature size may vary among the films, depending on the ratios of DMQA and DCV3T. In the 1:1 BHJ film, the efficiency of charge photogeneration was maximized, indicating that excitons of DMQA and DCV3T at this ratio have the highest probability of reaching dissociation sites among the three films. This implies that the interfacial area for exciton dissociation is largest in this particular BHJ film. DCV3T excitons, which have a relatively short lifetime (38–42 ps) compared to DMQA excitons (146 ps), require a smaller domain size in order to reach interfaces and dissociate before they decay back to the ground state. In case of the DMQA-rich film (3:1), the nanoscopic size of the DCV3T domains may be smaller than that of those in the DCV3T-rich film (1:3), suggesting that DCV3T excitons in the 3:1 film will survive long enough to reach dissociation sites and contribute more charge generation than in the 1:3 film. In addition, DMQA excitons with longer lifetimes may still contribute significantly to charge generation, even in the larger nanoscopic domains of the 3:1 film to give the higher relative carrier generation efficiency (0.79; *vide supra*) compared to that of 1:3 film (0.27). Therefore, it should be mentioned that the interfacial area, nanoscopic domain size, and exciton lifetime of DMQA and DCV3T are all key factors in the efficiency of charge photogeneration.

On the basis of the device characteristics and the analyses so far, a possible mechanism is proposed as the relatiionship between the device performance and the composition of the BHJ layer, in terms of absorption efficiency, charge transport, and charge carrier generation. The layer of blended DMQA and DCV3T with a ratio of 1:3 exhibited the highest absorption intensity, as shown in Figure II-4d, implying that it had the highest probability of exciton generation.[15] The excitons decayed rapidly within a time scale of 100 ps (Figure II-7b), before they had the chance to generate charge carriers.[15,23] The absorption efficiency of the DMQA/DCV3T 1:3 film was seen to be higher than that of the 3:1 film by a factor of 1.5, but the efficiency of charge generation was much lower in the 1:3 film. Further investigation into charge carrier mobility showed that the electrons move approximately two orders of magnitude faster than the holes in the 1:3 films (Table II-1). It has been suggested that the imbalance in carrier densities may also cause charge recombination and a consequent reduction in the charge collection efficiency,[16,17,20] resulting in a low zero-bias device EQE of 15.3% at 540 nm for the 1:3 film. Although the combined efficiency of charge generation and absorption was much higher than that in the 1:3 film, the 3:1 BHJ system, in which the hole mobility was two orders of magnitude higher than the electron mobility, demonstrated a reduced forward photocurrent density, as shown in Figure II-5. Although charge imbalance was observed in both the 3:1 and 1:3 ratios, it was clearly seen that the forward photocurrent density of the 3:1 BHJ system (faster holes) was significantly lower than

the 1:3 BHJ system (faster electrons), indicating that the electron mobility in the BHJ layer is the more significant factor in limiting the photocurrent density of the devices. Finally, the BHJ layer with a 1:1 ratio of DMQA/DCV3T showed relatively high absorption intensity, as shown in Figure II-4d, and also fairly efficient photon-to-charge generation (Figure II-7b). In addition, well balanced charge carrier mobility is likely to contribute to efficient charge collection, which in this case resulted in the highest zero-biased EQE of 27.5% at 540 nm for the 1:1 ratio.

II.4. Conclusion

It was investigated for the electrical and optical behaviours of BHJ films consisting of different ratios of DMQA (donor) and DCV3T (acceptor) molecules. Assessment of device performance demonstrated the highest EQE with a narrow band width occurred for the 1:1 ratio. The origin of this optimum composition was elucidated using light absorption, charge carrier photogeneration, and charge mobility analysis. Longer exciton lifetimes and smaller domain sizes guarantee more efficient photon-to-charge conversion, as was seen for the DMQA-rich film. However, a higher absorption coefficient means more incident light is utilized, as in the DCV3T-rich film. The balance between electron and hole mobility produces less charge accumulation and non-geminate recombination loss. All of these parameters have been shown to play important roles in overall device performance. A green-sensitive OPD constructed using this optimum composition realized a maximum EQE of over 67% at −5 V, demonstrating its great potential for application to CMOS image sensors.

II.5. Bibliography

1. Seo, H.; Aihara, S.; Watabe, T.; Ohtake, H.; Sakai, T.; Kubota, M.; Egami, N.; Hiramatsu, T.; Matsuda, T.; Furuta, M.; Hirao, T. *Jap. J. Appl. Phys.* **2011**, *50*, 024103.

2. Peumans, P.; Yakimov, A.; Forrest, S. R. *J. Appl. Phys.* **2003**, *93*, 3693-3723.

3. Mizuguchi, J.; Senju, T. *J. Phys. Chem. B*, **2006**, *11*0, 19154-19161.

4. Ziehlke, H.; Fitzner, R.; Koerner, C.; Gresser, R.; Reinold, E.; Bäuerle, P.; Leo, K.; Riede, M. K. *J. Phys. Chem. A*, **2011**, *115*, 8437-8446.

5. Dennler, G.; Scharber, M. C.; Brabec, C. *Adv. Mater*. **2009**, *21*, 1323−1338.

6. Uhrich, C.; Schueppel, R.; Petrich, A.; Pfeiffer, M.; Leo, K.; Brier, E.; Kilickiran, P.; Baeuerle, P. *Adv. Funct. Mater*. **2007**, *17*, 2991-2999.

7. Yan, H.; Swaraj, S.; Wang, C.; Hwang, I.; Greenham, N. C.; Groves, C.; Ade, H.; McNeill, C. R. *Adv. Funct. Mater.*, **2010**, *20*, 4329-4337.

8. Fitzner, R.; Reinold, E.; Mishra, A.; Mena-Osteritz, E.; Ziehlke, H.; Körner, C.; Leo, K.; Riede, M.; Weil, M.; Tsaryova, O.; Weiß, A.; Uhrich, C.; Pfeiffer, M.; Bäuerle, P. *Adv. Funct. Mater.*, **2011**, *21*, 897-910.

9. Paulus, E. F.; Leusen, F. J. J.; Schmidt, M. U. *Cyst. Eng. Comm.* **2007**, *9*, 131-143.

10. Sun, Y.; Welch, G. C.; Leong, W. L.; Takacs, C. J.; Bazan, G. C.; Heeger, A. J.

Nat. Mater. **2011**, *11*, 44-48.

11. Keivanidis, P. E.; Khong, S. H.; Ho, P. K. H.; Greenham, N. C.; Friend, R. H. *Appl. Phys. Lett.* **2009**, *94*, 173303.

12. Ng, T. N.; Wong, W. S.; Chabinyc, M. L.; Sambandan, S.; Street, R. A. *Appl. Phys. Lett.* **2008**, *92*, 213303.

13. Tedde, S. F.; Kern, J.; Sterzl, T.; Furst, J.; Lugli, P.; Hayden, O. *Nano Lett.* **2009**, *9*, 980-983.

14. Kim, J. S.; Lee, J. H.; Park, J. H.; Shim, C.; Sim, M.; Cho, K. *Adv. Funct. Mater.* **2011**, *21*, 480-486.

15. Clarke, T. M.; Ballantyne, A. M.; Nelson, J.; Bradley, D. D. C.; Durrant, J. R. *Adv. Funct. Mater.* **2008**, *18*, 4029-4035.

16. Mihailetchi, V. D.; Xie, H. X.; de Boer, B.; Koster, L. J. A.; Blom, P. W. M. *Adv. Funct. Mater.* **2006**, *16*, 699-708.

17. Lenes, M.; Morana, M.; Brabec, C. J.; Blom, P. W. M. *Adv. Funct. Mater.* **2009**, *19*, 1106-1111.

18. Binda, M.; Agostinelli, T.; Caironi, M.; Natali, D.; Sampietro, M.; Beverina, L.; Ruffo, R.; Silvestri, F. *Org. Electon.* **2009**, *10*, 1314-1319.

19. Mandoc, M. M.; Koster, L. J. A.; Blom, P. W. M. *Appl. Phys. Lett.* **2007**, *90*, 133504.

20. Koster, L. J. A.; Mihailetchi, V. D.; Blom, P. W. M. *Appl. Phys. Lett.* **2006**, *88*,

052104.

21. Cabanillas-Gonzalez, J.; Grancini, G.; Lanzani, G. *Adv. Mater.* **2011**, *23*, 5468-5485.

22. Stevens, M. A.; Silva, C.; Russell, D. M.; Friend, R. H. *Phys. Rev. B* **2001**, *63*, 165213.

23. Westenhoff, S.; Howard, I. A.; Hodgkiss, J. M.; Kirov, K. R.; Bronstein, H. A.; Williams, C. K.; Greenham, N. C.; Friend, R. H. *J. Am. Chem. Soc.* **2008**, *130*, 13653-13658.

Chapter III.

High Green-Sensitivity and Spectral Selectivity in Organic Photodetectors Using Subphthalocyanine Derivatives

III.1. Introduction

The sensitivity and spectral selectivity in targeted wavelength ranges are key factors of efficient image sensors. They can be expressed by analyzing the responsivity and crosstalk.

Crosstalk in an image sensor array results from three different contributions: spectral crosstalk due to imperfect color separation, optical spatial crosstalk induced by the transmission of unabsorbed light to an adjacent pixel, and electrical crosstalk by movement of the photo-generated carriers to the neighboring pixel.[1] Alternative candidates for the replacement of Si PD have been investigated for their high sensitivity with high absorption coefficient in order to reduce the optical and electrical crosstalk, simultaneously. However, most of inorganic semiconducting materials, due to their broad absorption spectra extending from the visible to the infrared (IR) region,

are not eligible for the color-selective photodetection.

Conjugated small organic molecules or polymers with their easily tunable absorption in the visible spectrum are interesting candidates as image sensor application. It was demonstrated that a hybrid CMOS-imager using P3HT:PCBM in a BHJ structure as an active layer suppressed the optical and electrical crosstalk due to the high coefficient of absorption of the polymer and the low-mobility in BHJ active layers, respectively.[2] However, the broad absorption between 400 nm and 650 nm of EQE spectrum still needs another color separation system for realization of color image. For the practical reduction of spectral crosstalk, the use of organic semiconducting small molecules with specific absorption ranges for respective RGB sub-pixels is promising for the replacement of Si PD. As the matierl with a narrow absorption in the wavelength region between 500 nm and 600 nm, boron-subphthalocyanine chlordie (SubPc) is an attractive candidate, which is introduced in Chapter I.3.3.

In this chapter, the highly green-sensitive OPD is demonstrated with a BHJ structure comprising SubPc derivatives and other materials mentioned in Chapter II for highly green-sensitive OPD. It was investigated by the electrical behavior and device efficiency of the OPD, from which the parameters of overall specific detectivity and spectral photoresponsivity were extracted. To interpret the spectral response of EQE spectra in detail, the photoresponsivities converted from EQEs are compared with the practical absorptions corrected by reflectances of the active BHJ layers. Finally, it

was performed by the calculation for the spectral crosstalk based on the model used in a conventional image sensor pixel arrays, and investigated the relationship between the sensitivity and spectral selectivity.[1]

III.2. Experimental

Materials. The molecular structures of the materials used in this study are shown in Figure III-1a. SubPc and N,N-dimethyl quinacridone (DMQA) were purchased from Lumtec Technology Corp., whereas pentafluoro-phenoxy substituted boron subphthalocyanine (F5-SubPc)[3] and dibutyl substituted dicyanovinyl terthiophene (DCV3T)[4] were synthesized according to the previous literatures, respectively.

Device fabrication: The organic photodiodes were fabricated on glass substrates pre-coated with indium-tin-oxide (ITO) with a sheet resistance of 15 Ω per square, as the anode. A 30 nm thick molybdenum oxide (MoOx) layer was further deposited on the ITO. And then, the organic BHJ layers with the thickness of 90 nm were deposited by vacuum thermal evaporation at a base pressure $< 2 \times 10^{-7}$ torr, and the composition ratios between a donor and an acceptor was controlled as same ratios at the deposition rate of 0.1 nm/s. The Al cathode was finally evaporated at a rate of 0.2 nm/s through a shadow mask with an active area of 0.04 cm^2. Four OPD devices with different

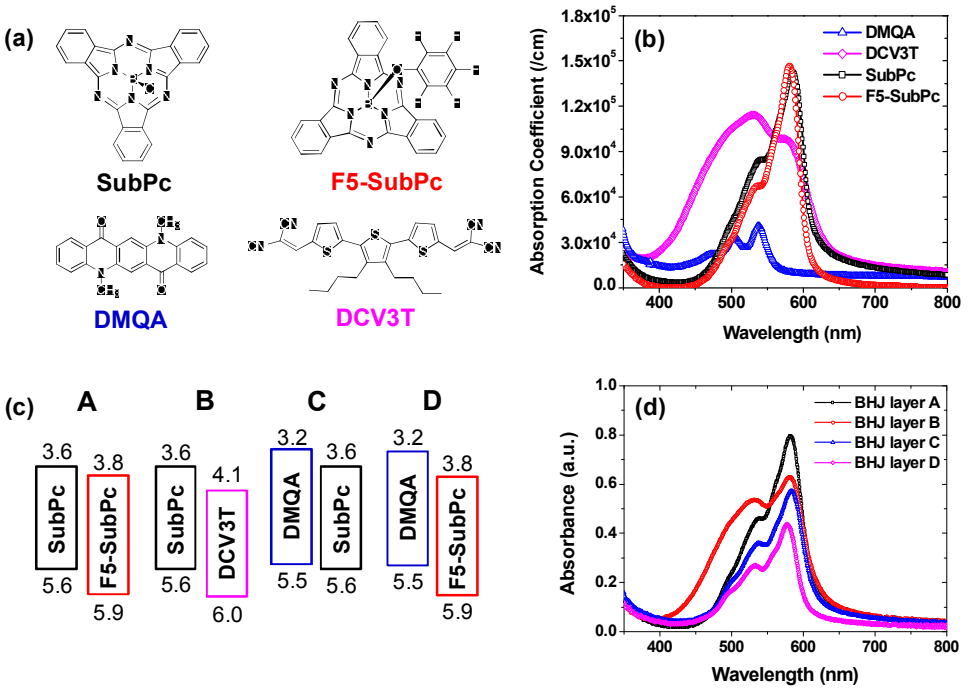

Figure III-1. (a) Molecular structures of Boron-subphthalocyanine chloride (SubPc), Pentafluoro-phenoxy-substituted SubPc (F5-SubPc), N, -N dimethyl quinacridone (DMQA) and Dibutyl-substituted dicyanovinyl terthiophene (DCV3T), (b) Absorption coefficients of four active materials measured by UV-Vis. Spectroscopy, (c) Energy level diagrams of donor/acceptor compositions for four basic OPD devices, and (d) Absorbance spectra of four BHJ.

donor/acceptor materials combination were fabricated: device A (SubPc / F5-SubPc), device B (SubPc / DCV3T), device C (DMQA / SubPc) and device D (DMQA / F5-SubPc). After cathode deposition, glass encapsulation was immediately performed under nitrogen by using a UV curable resin as sealant. The long-term device stability was monitored by measuring the current-voltage characteristics that did not change significantly over 6 months.

Device Characterization: The optical spectra of absorbance, transmittance and reflectance in the respective organic films grown on glass substrates were measured using a Shimadzu UV-240 spectrophotometer. The ionization potential of organic thin film was measured using by a photoelectron spectrometer in air (AC-2, RKI Instrument Co. Ltd.).

The charge transport characteristics of the individual materials were investigated by measuring the single carrier mobilities. The hole-only devices were fabricated by depositing a 30 nm MoOx film on the ITO-coated glass substrate, on top of which were deposited sequentially a 100 nm active layer, a 30 nm MoOx layer, an 80 nm Al electrode layer. The electron-only devices were prepared by the sequential deposition of a 100 nm active layer on the ITO, an ultrathin LiF layer and an Al cathode.

The external quantum efficiency (EQE) of OPD devises was measured using a spectral incident photon-to-current efficiency (IPCE) measurement system while illuminating monochromatic light generated by an ozone-free Xe lamp with a chopper frequency of

30 Hz. A calibrated Si-PD was used to measure the incident monochromatic light intensity. The current–voltage (*J–V*) curves were measured using a Keithley K4200 semiconductor parameter analyzer, and the light response was measured under illumination from a white LED with a broad range of emission wavelengths of 400 to 675 nm and light output intensity of approximately 1 mW/cm^2.

III.3. Result and Discussion

III.3.1. Highly Green-Sensitive OPD Using Subphthalocyanine Derivatives

Figure III-1b shows the film absorption spectra in the visible region of the different materials taken separately. SubPc shows the prominent lowest energy absorption band between the wavelengths of 560-600 nm, known as the Q-band resulting from the C3v symmetric ligand / molecular fragment.[5] The absorption spectra confirms high green color sensitivity of SubPc, with a maximum wavelength (λ_{max}) at 586 nm, a high absorption coefficient of approximately 1.4×10^5 cm^{-1} and a narrow full-width-at-half-maximum (FWHM) of 80 nm. Despite the change in electronic character, from p to n-type, the absorption spectra of F5-SubPc exhibits moderate variation as compared with SubPc, with a λ_{max} at 581 nm, a high absorption coefficient of 1.47×10^5 cm^{-1} and narrower FWHM of 49 nm. It was previously reported that axial substitutions on

SubPc make little effect on the shift of absorption band position.[6] DMQA shows low absorption with narrow FWHM, whereas DCV3T showed high absorption but relatively wide FWHM.[7-8]

The donor/acceptor compostions describing energy diagram are summarized in Figure III-1c. The potential of SubPc as a donor was first examined in combination with DCV3T and F5-SubPc as acceptors in devices A and B, respectively. Then, the possibility of using either SubPc or its derivative F5-SubPc as acceptors was evaluated by choosing DMQA as the donor, in device C and D, respectively. For the choice of donor and acceptor, it is necessary to consider the offset of lowest unoccupied molecular orbital (LUMO) levels between the two respective active materials. Except for composition A with an offset of 0.2 eV, all LUMO levels differences for the other device compositions were above 0.4 eV, which is sufficient for efficient charge separation.[9] Despite its small offset, device A has a potential for high EQE and good rectification, as shown in a previous study[5] in the field of OPV, where this composition was used to build planar heterojunction structures. In Figure III-1d, the absorbance spectra of all four BHJ films are consistent with the absorption coefficient spectra of the single active materials shown in Figure III-1b. Regarding the basic transport properties of these active materials, the charge mobilities measured by space-charge-limited-current (SCLC) model[10] are shown in the Table III-1.

The hole mobilities were similar for DMQA and SubPc with values of 1.62×10^{-8} and

Table III-1. Field-induced carrier mobility derived from the single carrier devices of active materials using the space-charge limited current model (electric field: 0.3 MV/cm).

Donor	h+ mobility (cm^2/Vs)	Acceptor	e- mobility (cm^2/Vs)
DMQA	1.62×10^{-8}	DCV3T	2.73×10^{-8}
SubPc	8.95×10^{-8}	SubPc	1.36×10^{-9}
		F5-SubPc	1.93×10^{-10}

8.95×10^{-8} cm^2/Vs at an applied electric field of 0.3 MV/cm, respectively, whereas the electron mobilities were different by orders of magnitude with values of 2.73×10^{-8} for DCV3T, 1.36×10^{-9} for SubPc and 1.93×10^{-10} cm^2/Vs for F5-SubPc. The difference in h+/e- mobilities for SubPc is consistent with the values reported in a previous study.[11] For the unambiguous characterization of the device performance, the structure of the OPDs was fabricated to be rather simple by avoiding the use of additional interlayers that could further complicate the analysis by introducing new interfaces in the system.

Before examining the device performances in details, the morphology of the different deposited thin films were investigated by atomic force microscopy (AFM). The analysis of surface morphology of the four neat films and four BHJ thin films are shown in Figure III-2 a-h. The pure SubPc, DMQA, and DCV3T films showed a root-mean-square (rms) roughness of 2.9 nm, 28.3 nm, and 17.4 nm, respectively, attributed to the significant self-aggregation resulting from their compact molecular structures.[12,13] Particularly, the corrugated surface morphology of SubPc thin film due to an horizontal growth behavior is consistent with a previous observation. [13] In contrast, the neat F5-SubPc film exhibited a smooth rms value of 0.38 nm, which is induced from the large fluoro-phenoxy group instead of chlorine in the axial position.

The surface roughnesses of four BHJ films were 0.39 nm, 0.41 nm, 13.57nm, and 5.59nm, respectively. It appears that two butyl groups in DCV3T or the bulky fluoro-

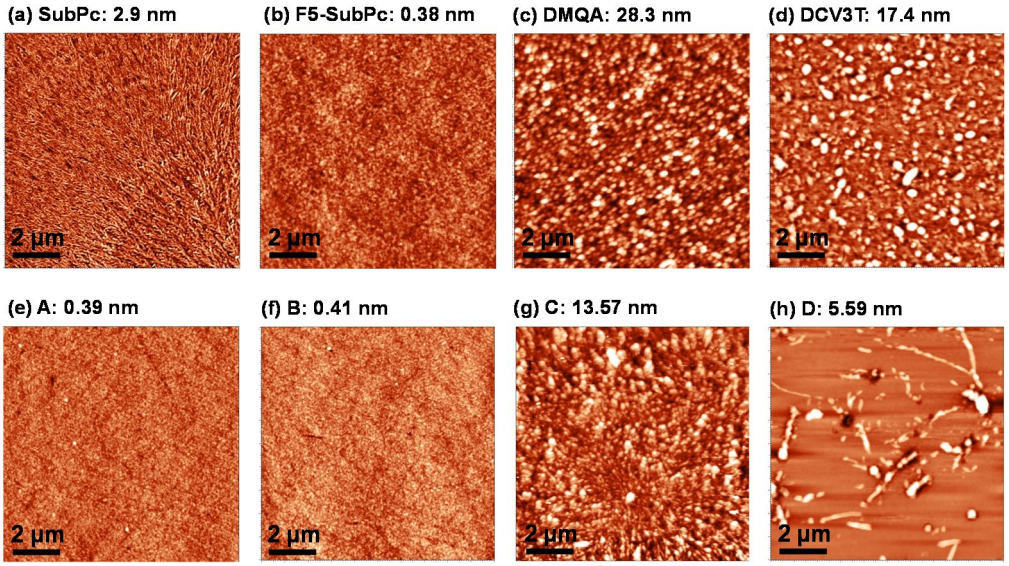

Figure. III-2. Atomic force microscopic topography of four neat films ((a) ~ (d)) and four BHJ films ((e) ~ (h)). The detailed descriptions are as follows; (a) neat SubPc, (b) neat F5-SubPc, (c) neat DMQA, (d) neat DCV3T, (e) A of SubPc / F5-SubPc, (f) B of SubPc / DCV3T, (g) C of DMQA / SubPc, and (h) D of DMQA / F5-SubPc. The field area of each film is 10 μm × 10 μm.

phenoxy group in F5-SubPc may lead to smooth blend morphology, while the character of DMQA with self-aggregation prevents the decrease in blend surface roughness. Therefore, the DMQA/SubPc thin film, without any amorphous regions, showed the coarser morphology, followed by DMQA /F5-SubPc thin films.

As the basic performances of the photodetectors, the current density–voltage (*J–V*) characteristics and the EQE spectra of the devices of A – D are shown in Figure III-3. The fundamental parameters of OPD devices are extracted from Figure III-3 and summarized in Table III-2. All devices exhibited similar levels of reverse dark current densities (J_d), within the same order of magnitude, from 4×10^{-8} A/cm^2 to 9×10^{-8} A/cm^2 at an applied voltage of -5 V. This particularly low J_d, considering the absence of any electron or hole blocking layers in the simple device structure, reflects the absence of leakage current. In this study on donor-acceptor compositions using the different four materials, the mophology differences of four BHJ films are not directly related with similar low J_d of four devices, which corresponds with the low relationship between the surface morphologies and the charge mobilities of four neat films.

Under illumination at a light intensity of 1 mW/cm^2, the photo-generated current densities (J_{ph}) of all four devices significantly increased by two orders of magnitude. However the ratio J_{ph} / J_d was different depending on the devices. The devices B and C exhibit relatively high J_{ph} / J_d ratios of 3.99×10^3 and 3.69×10^3, respectively, while the device A and D show relatively low J_{ph} / J_d ratios of 1.26×10^3 and 6.64×10^2 at

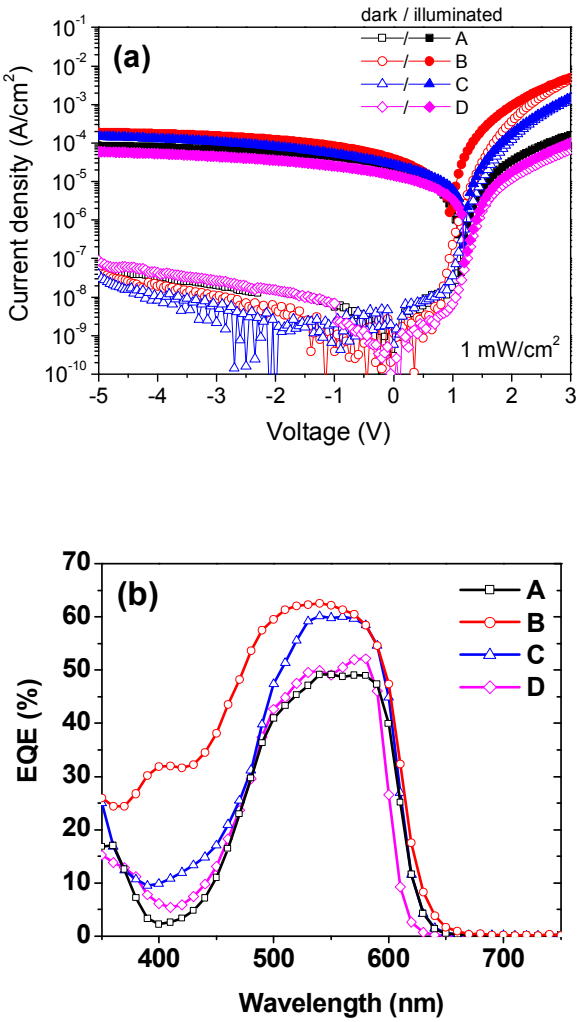

Figure. III-3. (a) Current density voltage characteristics in the dark and under illumination at 1 mW/cm^2 for four OPDs and (b) External quantum efficiency (EQE) spectra at an applied voltage of -5V. The device descriptions are as follows; (A) SubPc / F5-SubPc, (B) SubPc / DCV3T, (C) DMQA / SubPc and (D) DMQA / F5-SubPc as donors and acceptors, respectively.

Table III-2. Electrical parameters of the four OPD devices decomposed in terms of detectivity, sensitivity and spectral selectivity.

Device	Detectivity		Sensitivity		Selectivity	
	J_d	D^* @550nm	λ_{max}	EQE @ λ_{max}	EQE @450nm	FWHM
A	6.79×10^{-8}	1.48×10^{12}	550	49.2	11.0	137
B	5.31×10^{-8}	2.12×10^{12}	540	62.6	38.1	211
C	4.01×10^{-8}	2.34×10^{12}	560	60.1	17.1	131
D	8.99×10^{-8}	1.28×10^{12}	580	52.2	13.1	126

Abbreviations: Dark current density (J_d), Specific detectivity (D^*), Wavelength (λ_{max}), External quantum efficiency (EQE), and Full-width-at-half-maximum (FWHM).
Unit: J_d (A/cm^2), D^* (cm $Hz^{1/2}/W$), λ_{max} (nm), EQE (%), and FWHM (nm).

the applied voltage of -5 V, respectively. From the results of device B and C, it appears that SubPc can work as a donor or an acceptor, as long as energy levels are matched.[14] Additionally, the orders in J_{ph} / J_d ratios are consistent with the orders of forward photo-current densities, which are shown 5.00×10^{-3} A/cm^2 for B, 1.52×10^{-3} A/cm^2 for C, 1.61×10^{-4} A/cm^2 for A and 1.02×10^{-4} A/cm^2 for D at the applied voltage of 3 V, respectively. It has been reported that the forward current reduction under illumination influence the charge transport in devices composed of the same materials, resulting in variation in device efficiency.[10,15]

In addition, it was evaluated the specific detectivity as the green sensitivity parameter considering dark current noise, related with device efficiency, as shown in Table III-2. The specific detectivity (D^*) can be calculated from the expression of $D^* = (J_{ph} / L_{light}) / (2qJ_d)^{0.5}$, where J_{ph} is photocurrent density at the incident light intensity (L_{light}) at the wavelength of 550 nm and q is the absolute value of electron charge (1.6×10^{-19} C). Device C shows the highest value of 2.34×10^{12} cm• Hz$^{0.5}$/W owing to the high photo-current and low dark-current. The high D^* values over 10^{12} cm• Hz$^{0.5}$/W of all devices are comparable with the detectivity of photodetectors based on polymers or inorganic materials.[16,17]

To evaluate the spectral selectivity at the respective wavelength, the EQE plots of the four OPDs at the applied voltage of -5 V were measured, as shown in Figure III-3b. In the target wavelength range of green color, between 500 nm and 600 nm, the devices B

and C exhibited high EQE values of 62.6 % at the wavelength of 540 nm and 60.1 % at 560 nm, respectively, while the devices D and A showed relatively low values of 52.2 % at 580 nm and 49.2 % at 550 nm, respectively. Despite the EQE is a function of different interdependent factors, it is noted here that these EQE values correlate with the electron mobilities of individual materials taken as acceptors. It would imply that electron mobility, lower than the hole mobility, is the transport limiting factor. Meanwhile, the EQEs also show non-trivial intensity in the blue-color region between 400 nm and 500 nm, which may aggravate the spectral crosstalk. At the wavelength of 450 nm, device B showed the highest value of 38.1 % due to the broad absorption of DCV3T used as an acceptor, but the others devices also exhibited over 10 % EQEs despite the quite low absorption in the blue region of DMQA and SubPc-derivatives. The exact values of them extracted from Figure III-3b are presented in Table III-2. The FWHMs used as the simple index for the spectral selectivity[18] exhibited highest value of 211 nm for device B with best EQE, and secondly 137 nm for device A due to the low EQE value despite narrow absorption bandwidths of both donor and acceptor materials. It is noted that there is a conflict between the high EQE and the narrow FWHM. In the EQE spectra of Figure III-3b, it is interesting to note that λ_{max} at 550 nm is significantly shifted as compared to the highest absorption of SubPc derivatives at 580 nm, as shown in Figure III-1d. This is beneficial for the spectral sensitivity of a green-sensitive OPD.

III.3.2. Sensitivity and spectral crosstalk in OPD

To understand the difference between the EQE spectra of the OPD devices and the absorption spectra of the materials, it was analyzed by the optical properties of the four BHJ films including the transmittance, reflectance and absorbance that can be simply measured by UV-Vis spectroscopy. The term of absorbance is defined as the logarithmic ratio between the radiation falling upon a material and the radiation transmitted through a material, which is used as a conventional optical parameter of photopigment. In contrast, the absorptance is the absorption fraction out of the whole incident radiation flux, which complements the fractions of transmission and reflection.[19] Absorptance is thus the reflection-corrected absorption characteristics, which can be estimated by subtracting transmittance and reflectance from optical unity. The transmittance and reflectance spectra of four BHJ films are shown in Figure III-4.

In Figure III-5, the all absorptance spectra exhibit blunt shapes with a reduction of maximum absorption (Figure III-1d), which is induced from the reflectance effect. Whereas SubPc has proper property in terms of absorption, at 586 nm, the films comprising SubPc show high reflectance at the wavelength of 605 nm (Figure III-4b). The device D without SubPc showed the maximum reflectance at the wavelength of 594 nm (Figure III-4b), resulting in the same behavior but different peak position compared with other devices including SubPc, which implies that the high reflectance

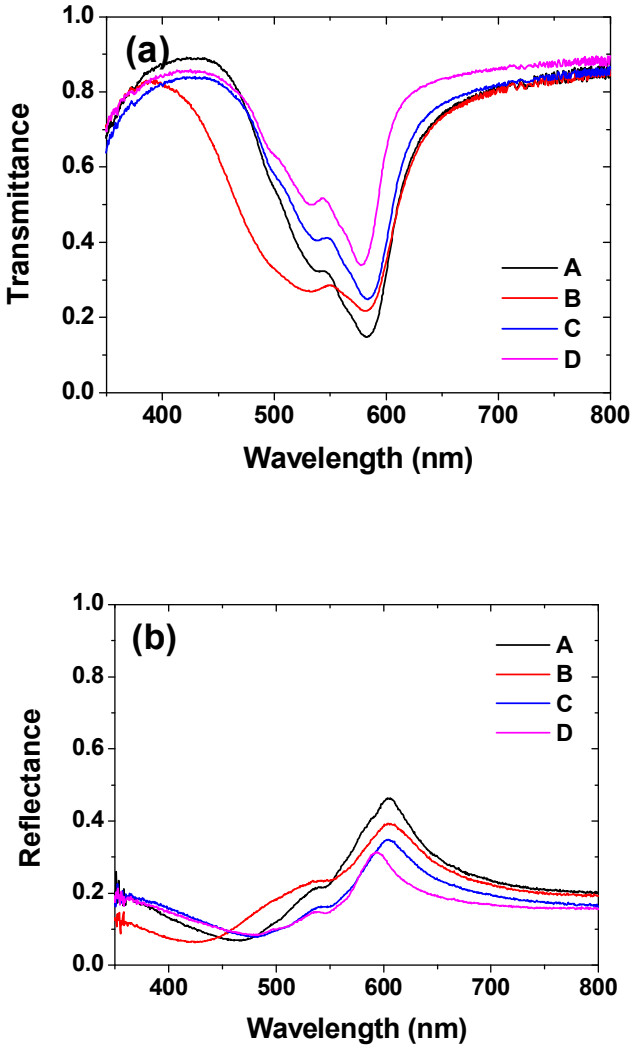

Figure III-4. The optical properties of (a) transmittance and (b) reflectance in four BHJ films on the glass substrate. The compositions of BHJ films are consisted of (A) SubPc / F5-SubPc, (B) SubPc / DCV3T, (C) DMQA / SubPc, and (D) DMQA / F5-SubPc, respectively.

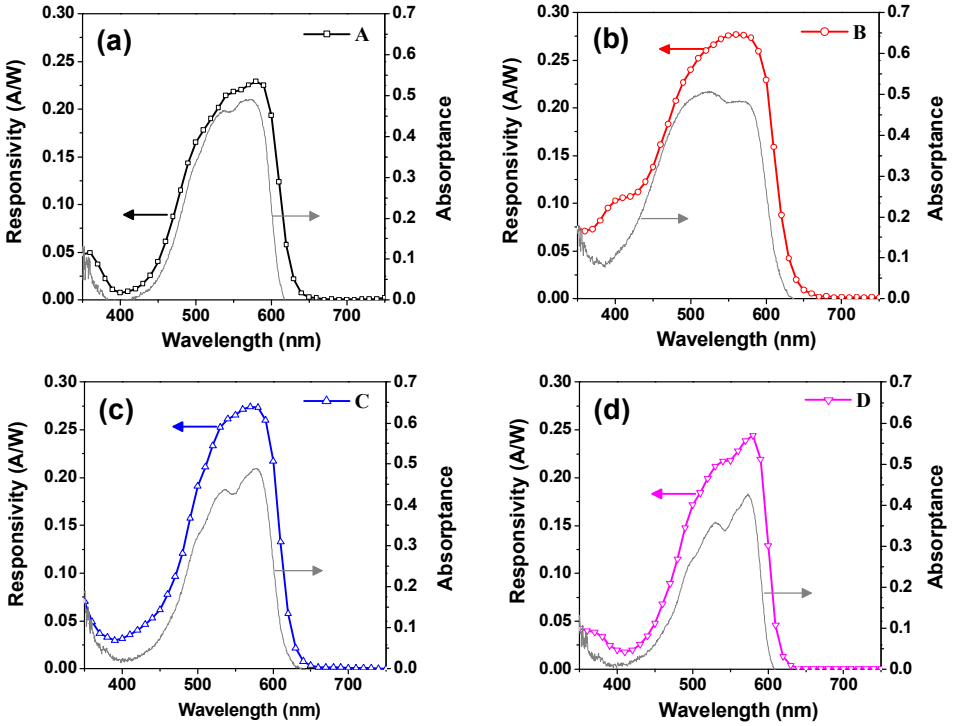

Figure III-5. The comparison between the photoresponsivity spectra of the OPD devices at an applied voltage of -5 V and absorptance spectra of four active BHJ films. The device descriptions are as follows; (a) A with SubPc / F5-SubPc, (b) B with SubPc / DCV3T, (c) C with DMQA / SubPc and (d) D with DMQA / F5-SubPc as donors and acceptors, respectively.

at 605 nm is caused by SubPc. With these practical absorption properties of BHJ layers corrected by reflections, the photoresponsivities were compared as the spectral sensitivities for the OPD devices, in Figure III-5. The photoresponsivity (R) is defined as R [A/W] = J_{ph} / L_{light} = EQE / hv, where hv is the energy of the incident photon in electron volts (eV).[16,20] For the devices A, C and D, the R profiles are consistent with the absorptance profiles, as the maximum peak intensity are located at the same wavelength. In contrast, the device B composed of SubPc and DCV3T shows a broader spectral responsivity with λ_{max} at 560 nm, which reflects that the absorptance is dominated by the absorption of DCV3T. The valley present around 540 nm in the absorptance spectrum is not visible in the photoresponsivity spectrum because of the applied bias voltage of -5 V. The R values could be simply converted to the EQE spectra, as shown in Figure III-3b, after correction with the photon energy of respective wavelength. Whereas the R values are similar in the blue and red regions, the EQE spectra show an amplified shoulder in the blue-region compared to that in the red-region due to the difference in photon energy.

In conventional image sensor arrays with color pixels, the spectral crosstalk usually corresponds to the ratio between the target signal (i.e. a signal in a green-absorbing pixel under green light illumination) and the undesirable signal (a signal in a green-absorbing pixel under blue- or red-light illumination). The signal is defined as the integral of photoresponsivity as spectral response at the specific wavelength region.[1]

Although the single color unit OPD is investigated in this study, the guide line for color selectivity is needed. Hence, it was examined the modified spectral crosstalk, which is defined as the ratio between the signal in green-region and the signal in blue- or red-region within a single responsivity spectrum. The specific wavelength regions are divided in blue (440-500 nm), green (510-570 nm), and red (590-650 nm) region according to conventional image sensor.

Figure III-6a shows the spectral responses by integrating the photoresponsivity within the specific wavelength regions, respectively. Among the four devices, the device B exhibits the highest integrated *R* value in the green region, however, with also pronounced *R* values in the blue- and red-region. In contrast, the device D showed a particularly low spectral response in the red region, as well as in the green region. In Figure III-6b, the green sensitivity-spectral crosstalk characteristics are represented by using the integral of *R* values in the green region and the ratio of integral values at blue/green regions and red/green regions. In terms of selectivity, the device D showed the lowest red crosstalk around 0.2, as the consequence of the presence of F5-SubPc, which induced an enhanced blue-shifted absorption in the blend film, as compared with SubPc. However, the green sensitivity of devices A and D are especially low. The sensitivity of device C is improved by around 17 % in comparison with device D, in result of the difference of maximum EQE values. In contrast, the device B shows the highest green-sensitivity with the desirable maximum peak position, even though the

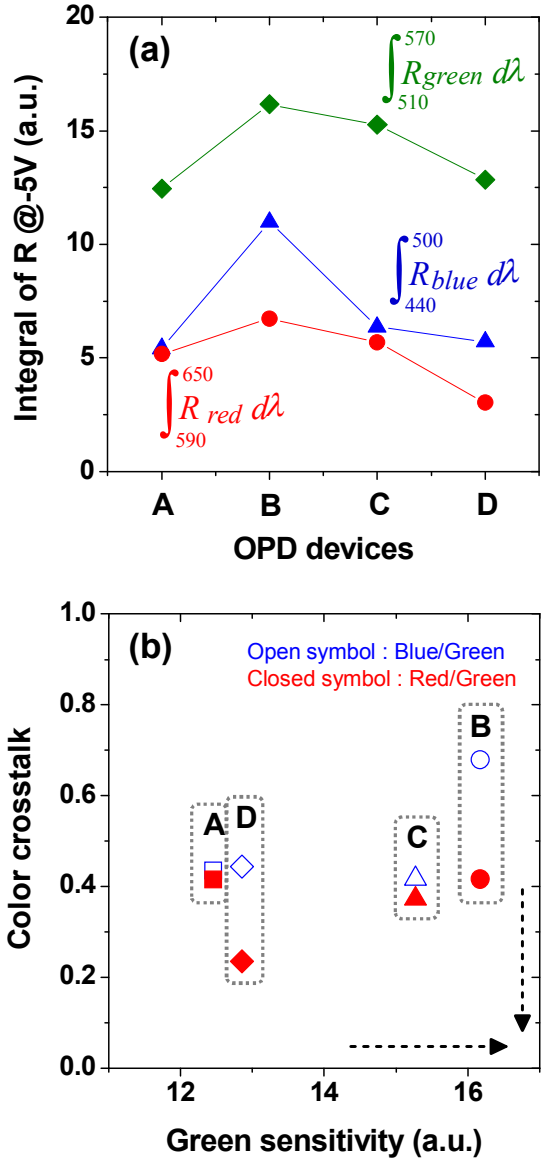

Figure III-6. (a) Spectral responses from the integral of responsivity within specific wavelength regions. (b) Green-sensitivity and spectral crosstalk of the four OPD devices.

blue sensitivity exhibits a factor of 0.7 of the green-sensitivity. From a comprehensive perspective, the device C exhibits optimized performance in term of high spectral sensitivity and selectivity.

To this point, on the basis of material properties and device characterization, it appears that it is difficult to achieve simultaneously high green-sensitive OPD with low blue crosstalk. High EQEs in the green-region have been reported in numerous devices, which however needed an additional color-filter for specific color recognition due to their wide band-width.[21-26] On the contrary, a device with narrow FWHM under 100 nm has been reported with an efficiency under 1 % at the applied voltage of -1.5 V.[27] It was reported that the blend layer thickness can be used to control the spectral selectivity, but may lead to limited sensitivity at high bias due to the absorption limitation of materials.[20] In this study, it is shown that SubPc derivatives are attractive material candidates for green-sensitive OPD with the merit of high absorption coefficient in the green-region and narrow FWHM. Additionally, the control of charge generation through proper energy levels and balanced charge transport is a prerequisite to achieve high sensitivity.[12] Considering these different aspects, it comes out the device C composed of DMQA and SubPc, characterized by reduced blue crosstalk with sufficient green-sensitivity, presents the ideal material combination for OPD application.

III.4. Conclusion

It was investigated the green-sensitive OPD with high spectral sensitivity and selectivity using SubPc derivatives for organic image sensor applications. The optimized composition is achieved by blending of DMQA as a donor and SubPc as an acceptor, and the performances exhibit the high D^* of 2.34×10^{12} cm $Hz^{0.5}$/W, the EQE value of 60.1 % at -5 V and small FWHM of 131 nm. In spite of sharp absorption property of SubPc with the λ_{max} at 586 nm, the spectrum of EQE showed the smooth waveform with λ_{max} at 560 nm as the favorable for high green sensitivity, which is induced from the high reflectance with λ_{max} at 605 nm. The highly green-sensitive OPD with low blue crosstalk is difficult to establish, nevertheless the device comprised of DMQA and SubPc realized the reduced blue-crosstalk and the highly green-sensitivity, demonstrating its promising potential for application to CMOS image sensors.

III.5. Bibliography

1. Agranov, G.; Berezin, V.; Tsai, R. H. *IEEE Trans. Electron Devices* **2003**, *50*, 4-11.

2. Baierl, D.; Pancheri, L.; Schmidt, M.; Stoppa, D.; Betta, G. –F. D.; Scarpa, G.; Lugli, P. *Nature Communications* **2012**, *3*, 1175.

3. Morse, G. E.; Helander, M. G.; Maka, J. F.; Lu, Z. –H.; Bender, T. P. *ACS Appl. Mater. & Interfaces* **2010**, *2*, 1934-1944.

4. Uhrich, C.; Schueppel, R.; Petrich, A.; Pfeiffer, M.; Leo, K.; Brier, E.; Kilickiran, P.; Baeuerle, P. *Adv. Funct. Mater.* **2007**, *17*, 2991-2999.

5. Morse, E.; Bender, T. P. *ACS Appl. Mater. & Interfaces* **2012**, *4*, 5055-5068.

6. Claessens, C. G.; Gonza´lez-Rodrı´guez, D.; Torres, T. *Chem. Rev.* **2012**, *102*, 835-853.

7. Mizuguchi, J.; Senju, T. *J. Phys. Chem. B* **2006**, *110*, 19154-19161.

8. Ziehlke, H.; Fitzner, R.; Koerner, C.; Gresser, R.; Reinold, E.; Bäuerle, P.; Leo, K.; Riede, M. K. *J. Phys. Chem. A* **2011**, *115*, 8437-8446.

9. Dennler, G.; Scharber, M. C.; Brabec, C. *Adv. Mater.* **2009**, *21*, 1323-1338.

10. Mihailetchi, V. D.; Xie, H. X.; de Boer, B.; Koster, L. J. A.; Blom, P. W. M. *Adv. Funct. Mater.* **2006**, *16*, 699-708.

11. Pandey, R.; Gunawan, A. A.; Mkhoyan, K. A.; Holmes, R. J. *Adv. Funct. Mater.* **2012**, *22*, 617-624.

12. Lee, K. –H.; Leem, D. –S.; Sul, S.; Park, K. –B.; Lim, S. –J.; Han, H.; Kim, K. –S.; Jin, Y. W.; Lee, S.; Park, S. Y. *J. Mater. Chem. C* **2013**, *1*, 2666-2671.

13. Kim, J.; Yim, S. *Appl. Phys. Lett.* **2011**, 99, 193303.

14. Beaumont, N.; Cho, S. W.; Sullivan, P.; Newby, D.; Smith, K. E.; Jones, T. S. *Adv. Funct. Mater.* **2012**, *22*, 561-566.

15. Lenes, M.; Morana, M.; Brabec, C. J.; Blom, P. W. M. *Adv. Funct. Mater.* **2009**, *19*, 1106-1111.

16. Gong, X.; Tong, M.; Xia, Y.; Cai, W.; Moon, J. S.; Cao, Y.; Yu, G.; Shieh, C. –L.; Nilsson, B.; Heeger, A. J. *Science* **2009**, *325*, 1665-1667.

17. Tedde, S. F.; Kern, J.; Sterzl, T.; Fürst, J.; Lugli, P.; Hayden, O. *Nano Lett.* **2009**, *9*, 980-983.

18. Vuuren, R. D. J.; Pivrikas, A.; Pandey, A. K.; Burn, P. L. *J. Mater. Chem. C* **2013**, *1*, 3532-3543.

19. Bass, M.; Van Stryland, E. W.; Williams, D. R.; Wolfe, W. L. *In Handbook of Optics* McGraw-Hill, New York, **1995**.

20. Leem, D. –S.; Lee, K. –H.; Park, K. –B.; Lim, S. –J.; Kim, K. –S.; Jin, Y. W.; Lee, S. *Appl. Phys. Lett.* **2013**, *103*, 043305.

21. Theil, J. A.; Snyder, R.; Hula, D.; Lindahl, K.; Haddad, H.; Roland, J. *J. Non-*

Cryst. Solids **2002**, *299-302*, 1234-1239.

22. Vygranenko, Y.; Chang, J. H.; Nathan, A. *IEEE J. Quan. Elec.* **2005**, *41*, 697-703.

23. Barton, J. B.; Cannata, R. F.; Petronio, S. M. *Proc. SPIE* **2002**, *4721*, 37-47.

24. Konstantatos, G.; Sargent, E. H. *Nature Nanotechnology* **2010**, *5*, 391-400.

25. Rauch, T.; Boberl, M.; Tedde, S. F.; Furst, J.; Kovalenko, M. V.; Hesser, G.; Lemmer, U.; Heiss, W.; Hayden, O. *Nature Photonics* **2009**, *3*, 332-336.

26. Gan, X.; Shiue, R. –J.; Gao, Y.; Meric, I.; Heinz, T. F.; Shepard, K.; Hone, J.; Assefa, S.; Englund, D. *Nature Photonics* **2013**, *7*, 883-887.

27. Fukuda, T.; Komoriya, M.; Kobayashi, R.; Ishimaru, Y.; Kamata, N. *Jpn. J. Appl. Phys.* **2009**, *48*, 04C162.

Chapter IV.
Dynamic Characteristics of the Green-Sensitive Organic Photodiode

IV.1. Introduction

Organic photodetector for application as image sensors has been developed by considering the static performance of EQE and spectral sensitivity, with few concerns on the dynamic frequency response, despite its critical importance to control optimal video capturing. A deep understanding on the mechanisms controlling the dynamic response of green-sensitive photodetectors based on non-fullerene small molecules is urgently needed to optimize the final performance of OPD for the image sensor application.

In this study, it was performed the dynamic electrical measurement on two different green-sensitive OPDs with similar static photo sensitivity, and calculated theoretical parameter based on the molecular structure, in order to link the dynamic properties of OPD devices to the molecular structure of the active materials. These two OPDs, characterized by excellent EQE values over 60%, are potential candidates for image sensors. The aim of this rearch is to differentiate these two devices based on their respective dynamic responses. In a first stage, the electrical parameters of the two

devices, including the resistance and capacitance, were extracted from impedance spectroscopy measurements, and then the carrier mobilities were estimated from the dynamic characterization. In a second stage, it was calculated the reorganization energy and the polarizability by simulation using Gaussian 09. These two properties are related to the charge mobility and dielectric constant, respectively. The calculated material properties corresponding to the device experimental data allowed to identify critical molecular features for the enhancement of frequency response, like aromatic ring fusion for charge mobility and the molecular geometry with isotropic net dipole for polarizability. From this systematic study combining electrical analysis and molecular simulation, a guideline for materials design of organic small molecule as alternatives to the fullerene derivatives is suggested to achieve high performance OPD in terms of dynamic characterization of OPD.

IV.2. Experimental

Materials: The molecular structures of the materials used in this study are shown in Figure IV-1 (a). N,N-dimethyl quinacridone (DMQA) (Lumtec, > 99% purity) was used as the common donor, whereas dibutyl-substituted dicyanovinyl terthiophene (DCV3T) (>99% purity) and boron-subphthalocyanine chloride (SubPc) (Lumtec, > 99%

purity) were used as two different acceptors for device A and B, respectively.

Device fabrication: The simple device structure with bulk hetero-junction (BHJ) active layer is shown in Figure IV-1b, and the detailed fabrication procedure is performed by the experimental description of Chapter III. Briefly, a 30 nm thick molybdenum oxide (MoO_x) layer was deposited on the indium-tin-oxide (ITO) coated glass substrate with a sheet resistance of 15 Ω per square, and an Al cathode with the thickness of 80 nm was evaporated at a rate of 0.2 nm/s through a shadow mask with an active area of 0.04 cm^2 after depositing the active materials. The organic BHJ layers with the thickness of 90 nm were deposited by vacuum thermal evaporation at a base pressure < 2×10^{-7} torr, and the composition ratios between the donor and the acceptor was kept constant at the same deposition rate of 0.1 nm/s. The devices thickness was optimized to get the respective external quantum efficiency (EQE) and dark current density level in the same range. The two OPD devices are referred to as device A for DMQA / DCV3T and device B for DMQA / SubPc.

Device characterization: The current density–voltage (*J–V*) characteristics were measured using a Keithley K4200 semiconductor parameter analyzer, and the EQE was measured using a spectral incident photon-to-electron conversion efficiency (IPCE) measurement system under monochromatic light generated by optical filter from an ozone-free Xe lamp with a chopper frequency of 30 Hz. A calibrated Si-PD was used to

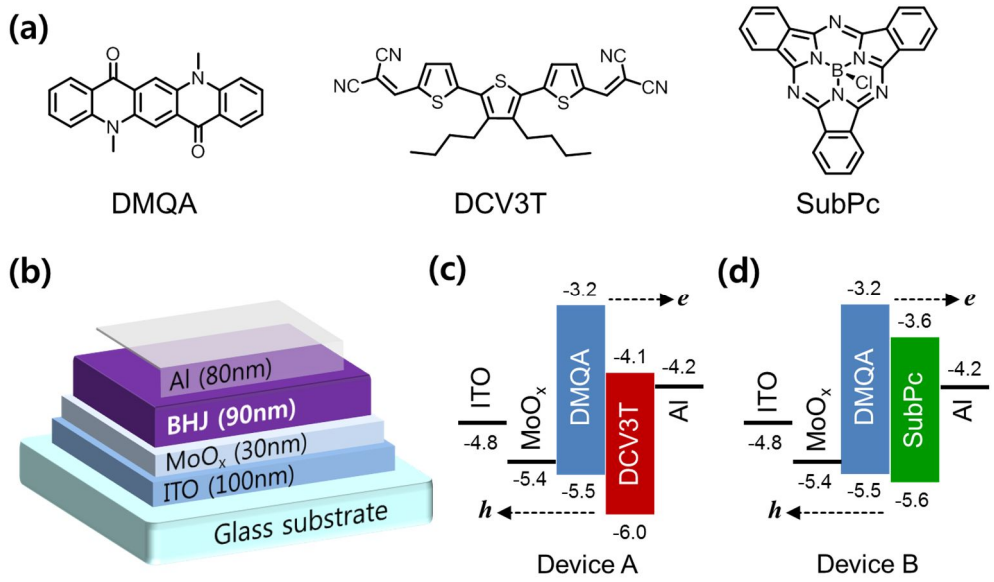

Figure IV-1. (a) Molecular structures of the organic molecules used for active bulk heterojunction (BHJ) layer comprising the donor of N,N-dimethyl quinacridone (DMQA), and two acceptors of dibutyl-substituted dicyanovinyl terthiophene (DCV3T) and boron-subphthalocyanine chloride (SubPc). (b) Schematic representation of the OPD device structure and energy level diagram of device components for (c) device A (DMQA/DCV3T) and (d) device B (DMQA/SubPc).

measure the incident monochromatic light intensity

The measured incident light power was 176 μW/cm^2 at the wavelength of 540 nm. The frequency response of photocurrent was evaluated using the measurement setup consisting of a 500-MHz bandwidth oscilloscope (Le Croy Wavejet 352A), a AFG-2125 function generator (GW instek), and a green laser diode (λ=553 nm, 10 mW/cm^2). The single pulse responses of the two devices were measured at the condition applying a single light pulse with ignition at 200 μs and a pulse width of 1 ms at an input intensity of 85 μW. The rise (decay) time is defined as the time needed to change the photocurrent intensity from 10 % (90 %) to 90 % (10 %).[1] Impedance spectroscopy measurements were carried out with a Solartron 1260 impedance analyzer with the frequency sweep range from 10 to 10^6 Hz. The alternating current (AC) oscillator level was set to 100 mV. The light source is a green-LED with an intensity of 1 mW/cm^2.

IV.3. Result and discussion

IV.3.1. Analysis of dynamic properties related with the frequency response

All materials, shown in Figure IV-1a, have a maximum absorption peak located between 500 nm and 600 nm, suitable for green-color sensitivity.[2] Even though the

number of organic semiconductors combining a n-type character with green absorption are rare, it could be found two acceptor materials satisfying both criteria. In device A, DCV3T possesses the acceptor-donor-acceptor (A-D-A) sequence consisting of a linear conjugated terthiophene backbone and dicyanovinyl groups at each extremities.[3] The n-type character of DCV3T lies in the strong electron-withdrawing character of the cyanovinyl groups and the relatively short conjugation length of the donating terthiophene backbone.[4] DCV3T was thus used as an acceptor in earlier studies, as summarized in Chapter I.3.2. In device B, the high absorption of SubPc between 560 and 600 nm is the consequence of *Q*-band formation induced by the C3v symmetric ligand/molecular fragment arrangement.[5] This is directly linked to the specific cone shape of SubPc composed of three *N*-fused diiminoisoindole units terminated by a tetracoordinated boron (B) at the angular point and chlorine (Cl) in the axial position.[6] For evaluating the effect of two different acceptors, DMQA was set as the common donor material in this study. DMQA shows proper LUMO energy level offsets over 0.4 eV in combination with either DCV3T or SubPc for guarantying efficient charge separation, as shown Figure IV-1c and IV-1d.[7]

Figure IV-2 shows the static response for the *J-V* characteristics and the EQE spectra of the two OPDs. As shown in Figure IV-2a, both devices exhibit similar levels of dark current densities (J_d) of 3.7×10^{-8} A/cm^2 for A and 1.2×10^{-8} A/cm^2 for B at an applied voltage of -5 V. In spite of the simple device structure, the leakage current in the dark

was not significant owing to the electron blocking effect of the MoOx layer.[8] Figure IV-2b, which shows the EQE spectra at an applied voltage of -5 V for the two devices, highlights the practically good and mutually comparable performance of both materials with similar EQE values of 60.7 % for the device A and 60.1 % for device B at the same maximum wavelength of 540 nm. The equivalent EQE values, which correlate to the number of charge carriers converted from incident photons, are a sign of similar charges concentrations in device A and B at this specific wavelength.

Figure IV-3 shows the dynamic characterization of the two devices, including the response times and cut-off frequencies of photocurrent. First, the single pulse responses of the two devices were measured. The rise times (τ_r) and decay times (τ_d), calculated from the normalized photocurrent, were respectively 12.2 μs and 12.5 μs for device A, and 6.6 μs and 7.5 μs for device B, as shown in Figure IV-3a. The cut-off frequencies at an applied voltage of -5 V bias were 92.9 kHz for device A and 148.3 kHz for device B, from Figure IV-3b. In contrast to the static performance, the difference in the dynamic response between the two devices was substantial.

Considering the high EQE over 60% and the imaging speed above 100 kHz, device B can be regarded as a potential candidate for image sensor.[9] The significant difference of frequency bandwidth between the two devices is maintained from zero bias to a reverse bias of -10 V, as shown in Figure IV-3c. In spite of similar static performances, the dynamic responses of the two devices are thus significantly different to motivate

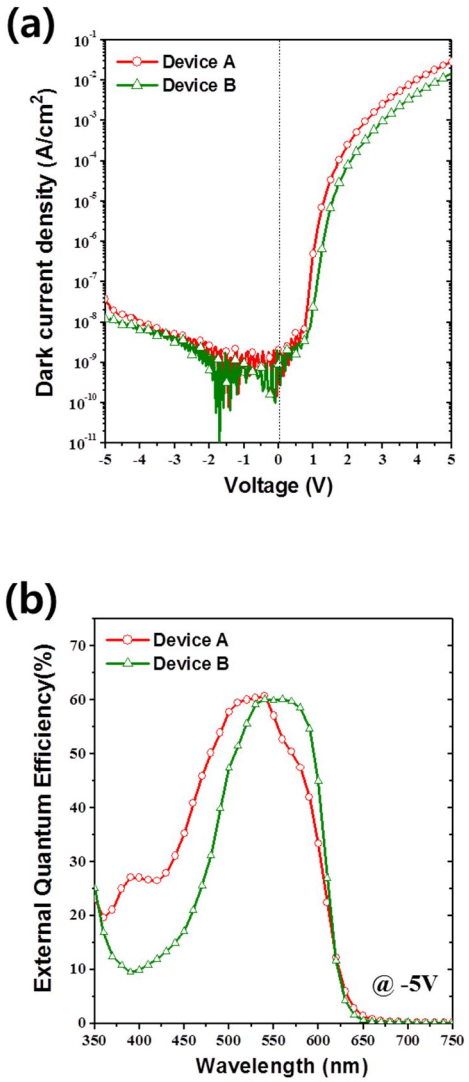

Figure IV-2. (a) Current density-voltage (*J-V*) characteristics, and (b) external quantum efficiency (EQE) spectra for the two green-sensitive OPDs at the applied voltage of -5 V.

further analysis of the electrical parameters.

Impedance spectroscopy gives an estimation of the electrical parameters of resistance and capacitance by modeling the OPD with an appropriate equivalent circuit based on the device structure. It was measured the two devices in the dark and under illumination using a green-LED with a maximum wavelength of 532 nm and the intensity of 1 mW/cm^2 at the direct current (DC) bias of -5 V, as shown in Figure IV-4a and IV-4b. In the dark, the curves steadily increase, which would ultimately form a large semi-circle above the MΩ range. In contrast, the spectra under illumination exhibit an almost complete semi-circle within dozens of kΩ range. Considering the simple device structure, the equivalent circuit shown in the inset of Figure IV-4a was used as model.[10] The equation for the impedance is derived as follows;

$$Z = R_1 + \frac{1}{1/R_2 + i\omega C_1} \qquad \text{(eq. 5)}$$

where R_1 is the sheet resistance through a MoO_x hole transport layer, R_2 and C_1 are the resistance and capacitance of the active BHJ layer, respectively. R_1 contribute to a small portion of the total resistance only, between 90 Ω and 160 Ω, regardless of the measurement conditions. It can be neglected as compared with R_2, which reaches the respective estimated values of 1.35×10^7 Ω for device A and 2.28×10^7 Ω for device B in the dark. These values were obtained from the analysis of the experimental curves shown in Figure IV-4a. The resistances in the dark mainly result from the leakage

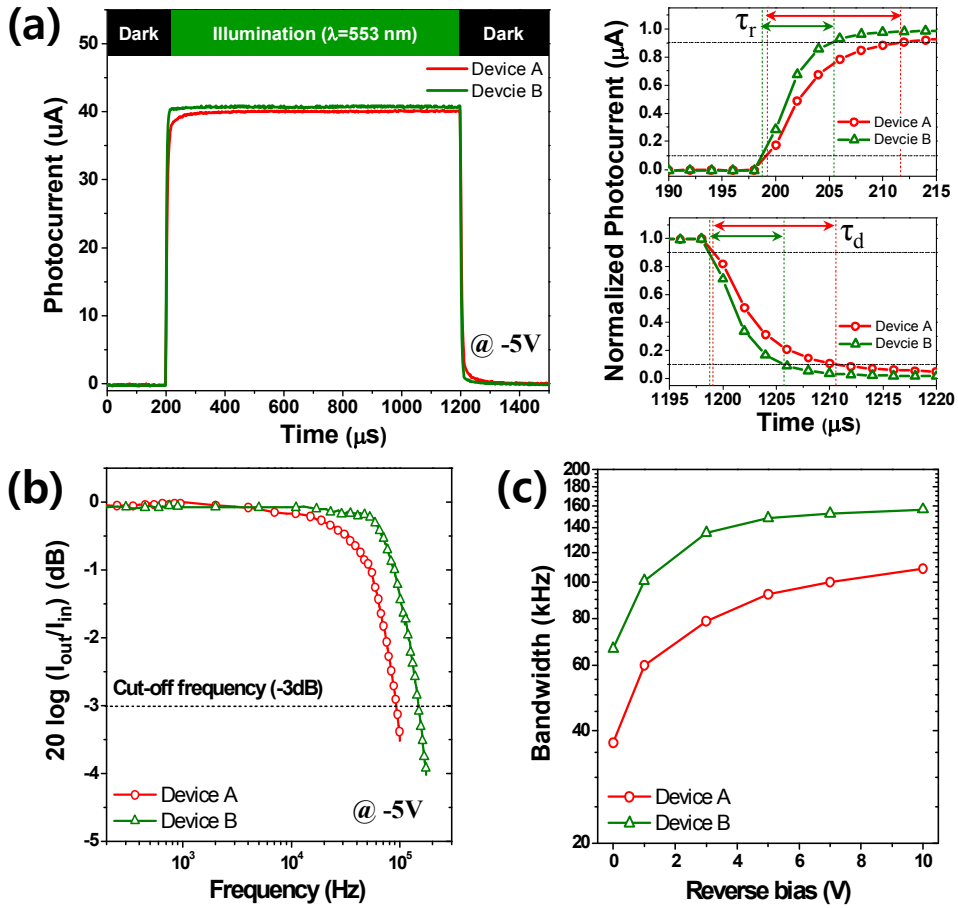

Figure IV-3. (a) Single light pulse response at a light intensity of 85 μW and a wavelength of 553nm. The inset highlights the rise times (τ_r) of 12.2 μs for device A and 6.6 μs for device B (above), and the dacay times (τ_d) of 12.5 μs for device A and 7.5 μs for device B (below), (b) cut-off frequency at the applied voltage of -5V of the two BHJ OPDs, and (c) bandwidth for frequency response of the OPDs under reverse bias.

current, which is consistent with the dark current density of *J-V* curves shown in Figure IV-2a. Under illumination as extracted from the experimental data shown in Figure IV-4b, the R_2 resistances are significantly reduced to 4.50×10^4 Ω for device A and 2.82×10^4 Ω for device B. In terms of conductivity, taken as the reciprocal of resistance, the dark current densities in both devices are minor as compared to the photo-generated currents. Regarding the capacitances, the respective C_1 values remained unchanged in the dark or under illumination, at 2.3 nF for device A and 1.9 nF for device B. It is inferred that all photo-generated carriers reach both respective electrodes without accumulation or recombination because of the applied voltage of -5 V as reverse bias, resulting in the preserved capacitance. The different capacitance values between the two devices logically originate from the different dielectric constants of 4.37 for BHJ layer A and 3.69 for layer B, which were measured from simple device structures composed of the BHJ active layers only, without any interlayers. The electrical parameters evaluated from Figure IV-4 are summarized in Table IV-1. From these results, it appears that the higher frequency photo-response of device B is the consequence of the lower resistance and the lower capacitance at the applied voltage of -5 V. It is now necessary to clarify the origin of the lower resistances through the experimental evaluation of mobilities.

Recently, it was reported that the average charge mobility in practical OPDs can be obtained by measuring the impedance under applied forward bias voltage.[11] In this

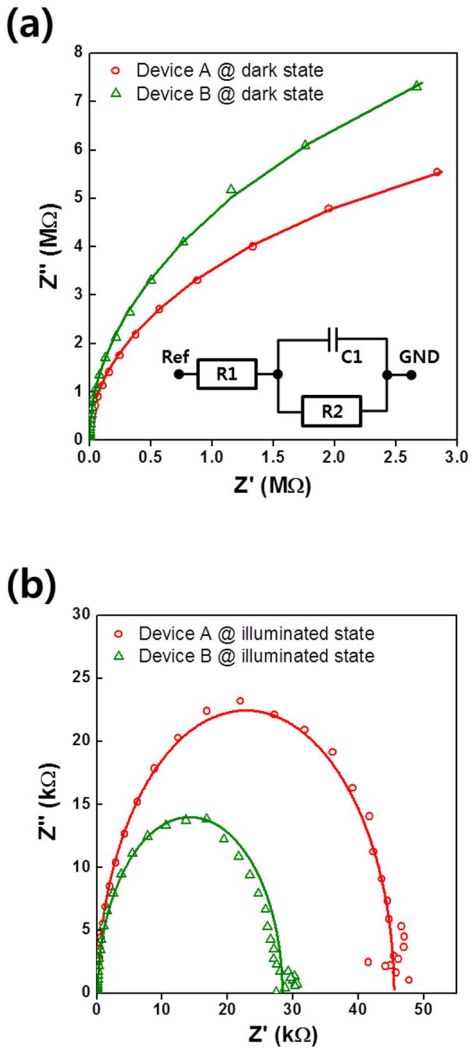

Figure IV-4. Impedance spectra measured (a) in the dark and (b) under illumination with a green-LED at an intensity of 1 mW/cm^2 and a wavelength of 532nm at the applied voltage of -5 V. The inset shows the equivalent circuit used to model the impedance. Solid lines show the fitting to the equivalent circuit.

method, the imaginary part of impedance (Im Z) peak is quite stable even in the presence of a moderate degree of dispersion, and the transit time corresponding to the average charge carrier mobility can be derived. Assuming AC mobility with no dispersion, which means that the AC mobility normalized to DC mobility is unity, the frequency dependence of admittance is given by[11]

$$Y(\Omega) = \frac{1}{Z(\Omega)} = \frac{\varepsilon A}{\tau_{dc} d}\left(\frac{\Omega^3}{2i(0.75)^2\{1-\exp[-4i\Omega/3]\}+1.5\Omega - i\Omega^2} \right) \quad \text{(eq. 6)}$$

where $\Omega = 2\pi f \tau_{dc}$, f is the frequency, and τ_{dc} is the DC transit time. Figure IV-5 shows the curves of Im $Z(f)$ curves of the two devices in the dark at the forward bias of 5 V. By referring to the above equation, fitting to the equivalent circuit shown in inset of Figure IV-4a was performed, and the transit times were extracted as 7.6 μs and 5.8 μs for devices A and B, respectively. The average charge carrier mobilities of devices A and B were respectively 2.8×10^{-6} and 3.7×10^{-6} cm^2/Vs, obtained from the extracted transit time using $\mu_{dc} = 4L^3/(3\tau_{dc}E)$, where L is the thickness of organic layer and E is the electric field.[12] Despite the discrepancy between the measured and fitted values due to the assumption of an AC mobility without dispersion, the difference levels remain similar for two devices. It is also noted that the peak frequency values of Im Z match well with the fitting data. These results demonstrate that the average carrier mobility in device B is higher than that in device A. From the references on the relation

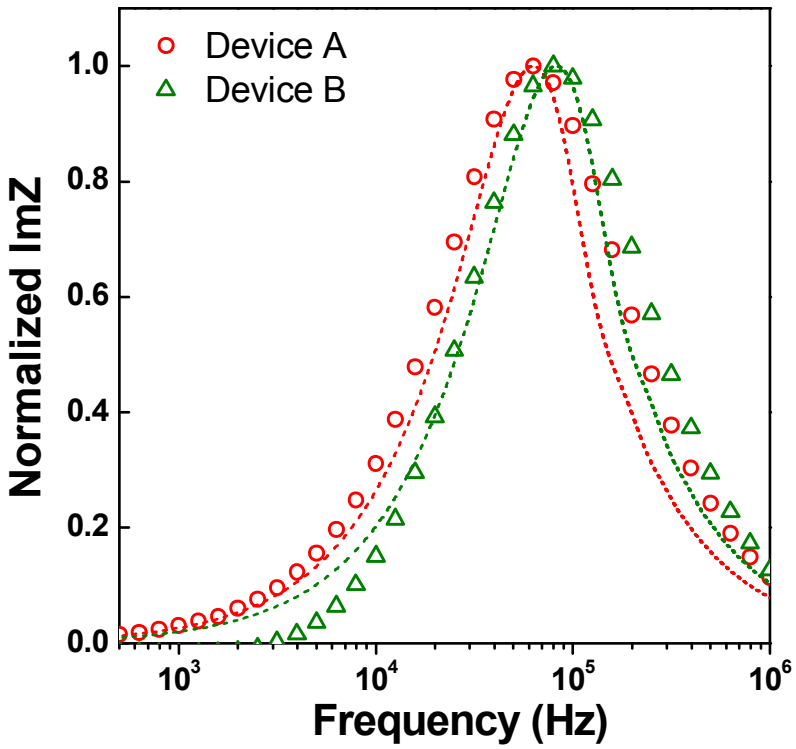

Figure IV-5. Frequency dependency of imaginary part of impedance (Im Z(f)) of the two devices at the forward bias voltage of 5 V.

between frequency response and carrier mobility,[13] it can be inferred that the charge mobility is the main limiting factor for the dynamic response, considering the similar charge concentrations in the two devices. From the collected experimental data, the faster frequency response of device B, as compared with device A, might result from the lower capacitance and higher conductivity. These two respective properties are directly linked to the dielectric constant and charge mobility of the materials. Since they are inherent material properties, their estimation from their molecular structures would allow to get a direct prediction of the device dynamic response and to find directions to improve the dynamic parameters.

IV.3.2. Correlation between molecular calculation parameters and electrical properties

As the important parameter governing the frequency response, the charge transport theoretically depends on the two following contributions: the transfer integral as the intermolecular electronic coupling and the reorganization energy as the intramolecular vibronic coupling.[14,15] The first contribution, related to the relative arrangement of the molecules in the crystal state, has been deeply considered for the characterization of mobility in organic field-effect transistors (OFETs) based on the single crystal molecular structure.[16] In OPDs, the active layer exhibits an amorphous BHJ structure

Table IV-1. Electrical parameters of resistance and capacitance obtained from the fit of Figure IV-4, the average mobilities derived from the Figure IV-5, and the dielectric constant values, respectively.

		Device A (DMQA/DCV3T)	Device B (DMQA/SubPc)
Resistance R_2	dark	1.35×10^{7}	2.28×10^{7}
(Ω)	illuminated	4.50×10^{4}	2.82×10^{4}
Capacitance C_1	dark	2.26	1.89
(nF)	illuminated	2.29	1.87
Dielectric constant		4.37	3.69
Average mobility (cm^2/Vs)		2.8×10^{-6}	3.7×10^{-6}

built by co-deposition of a donor and an acceptor molecule. The transfer integral contribution is thus not quantifiable in such a system. The second contribution for carrier mobility, the reorganization energy, is the energy change of a single molecule on charge addition/removal. It can be controlled by increasing the conjugation length[17] and by chemical substitution on the molecular structure.[18] The capacitance is another critical parameter to be considered, as it delays RC in frequency response. The capacitance is affected by the relative permittivity (ε) of the material, which depends on the polarizability (*P*) of the molecule.[19] The calculation of *P* has been used to predict the optical birefringence of nematic liquid crystals.[20] To this date, the complete figure showing the correlation between the dynamic performance of the device and the molecular characteristics of the materials is however still needed.

To correlate the intrinsic materials properties with the dynamic device parameters in these OPDs, it was simulated the electronic properties including the reorganization energy of the two individual acceptor molecules, and the polarizability of two pairs of molecules by random sampling. The results of simulation are shown in the Table IV-2, using Gaussian 09 at the DFT B3LYP level with 6-31g(d,p) basis set.[21] The hole reorganization energies (λ_h) is 0.262 eV for DCV3T and 0.095 eV for SubPc, which corresponds with the feature of SubPc with low reorganization energy.[22] In case of the electron reorganization energy, λ_e of DCV3T with the value of 0.335 eV is larger than that of SubPc at 0.283 eV. These data are consistent with the measured charge

mobilities in Figure IV-5. The lower values of SubPc might originate from its fused structure as compared with the conjugated backbone structure with conformational torsion points of DCV3T.

The dipole moments and polarizabilities were then calculated in dimer packing configuration, as shown in Figure IV-6. The optimized configuration was obtained by selecting the pair with minimum interaction energy among arbitrarily generated configurations by using the Blends module with DREIDING forcefield in Materials Studio package.[23] For the calculation, energetically favorable configurations were predominantly obtained by using a sampling technique based on the excluded-volume constraints method[24] and the molecular Silverware algorithm.[25] The average dipole moments in all directions, reported in Table IV-2, are 1.1 D for both dimer molecules.

The dipole of DCV3T in the conjugation direction might mutually vanish due to the balance between two accepting dicyanovinylene units, and the dipole moments by alkyl groups at the orthogonal direction can be also reduced, as interpreted from the analysis of the molecular configurations shown in Figure IV-6a and IV-6b. SubPc possesses a net dipole in the axial B-Cl direction only, due to the symmetry of the three-branched *N*-fused diiminoisoindole in the molecule periphery. Therefore, SubPc dimers have a tendency of favorable packing to counterbalance the B-Cl dipole moment,[6] as illustrated by the bi-molecular packing orientations shown in Figure IV-6c and IV-6d. The calculated polarizabilities for the induced dipole moment considering

Table IV-2. Simulated parameters of DCV3T and SubPc calculated by Gaussian 09 at the DFT B3LYP level with 6-31g(d,p) basis set.

	HOMO	LUMO	E_g	S1 (λ_{max})	λ_h	λ_e	|D|*	|α|*
DCV3T	5.992	3.369	2.623	2.43 (509)	0.262	0.335	1.1	1881.2
SubPc	5.312	2.589	2.723	2.52 (492)	0.095	0.283	1.1	969.8

Abbreviations : highest occupied molecular orbital (HOMO), lowest occupied molecular orbital (LUMO), energy gap (Eg), singlet state (S1), hole reorganization energy (λh), electron reorganization energy (λe), absolute value of dipole moment at the optimized dimer packing (|D|, debye [D]), absolute value of polarizability at the optimized dimer packing (|α|, atomic unit [au])

* The dimer packing structures are calculated using Blends modules with DREIDING force field in Materials Studio V 7.0.

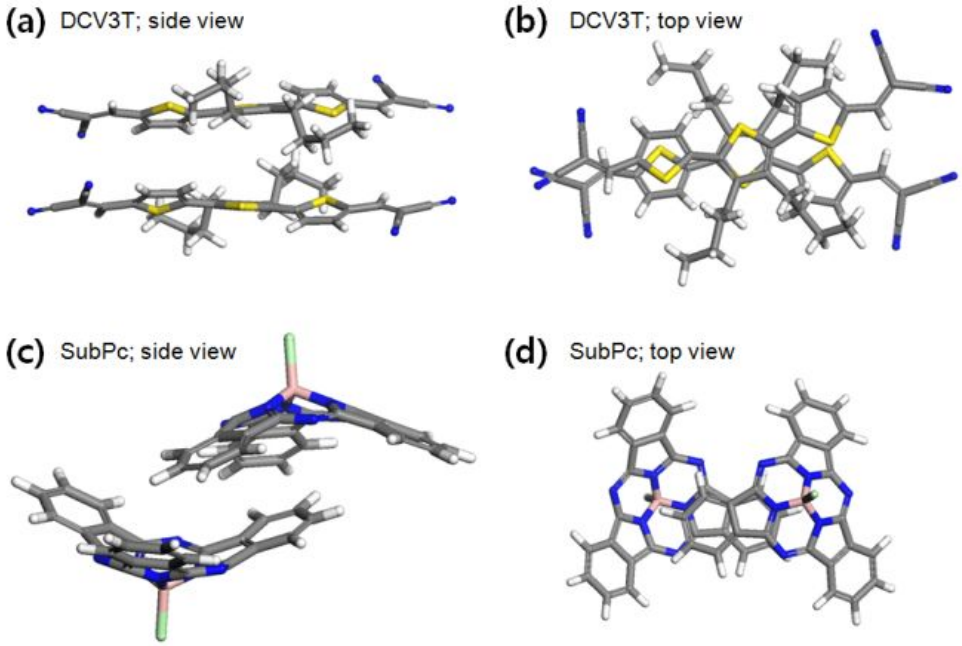

Figure IV-6. Dimer packing structures for two acceptors calculated using Materials Studio: (a) and (b) DCV3T, (c) and (d) SubPc.

molecular packing are 1881.2 au for DCV3T and 969.8 au for SubPc. The overall polarization of SubPc might vanish in random configuration considering no net dipole by dimer packing, even in the bulk state. In contrast, the linear structure of DCV3T with the A-D-A sequence may promote packing in the linear direction,[4] so that the polarizability could be maintained. These polarizability calculations based on molecular geometry are consistent with the dielectric constant values measured in the respective BHJ layers, explaining the influence on the capacitances.

The comparison between materials simulation data and experimental device results allows to suggest a few critical points related to the material molecular structures to obtain an OPD device with fast dynamic response. The first point is a fused aromatic structure, related to charge carrier mobility of the device, and the second point is the molecular geometry with isotropic net dipole, related to the capacitance of the device. In addition to the improvement of mobility, prohibiting conformational torsions by conjugated-ring fusion might lead to a decrease of absorption band-width,[26] which is favorable for specific color-sensitive OPD in image sensor application. Following these material design criteria might help to identify small molecules pairs for BHJ for the device with high dynamic response, in a first stage comparable with devices based on fullerene, and eventually comparable to inorganic semiconductors.

IV.4. Conclusion

The different dynamic frequency responses of two OPDs based on non-fullerene small molecules with similar static photo sensitivities have been investigated. The faster frequency response of 148.3 kHz at -5V bias voltage of device B (DMQA / SubPc) originates from the low resistance and capacitance measured by impedance analysis, as compared with 92.9 kHz of device A (DMQA / DCV3T). The lower resistance is due to the higher mobility, while the lower capacitance is linked to the relatively low dielectric constant. The calculated reorganization energy and polarizability of the two different acceptors, which are theoretical parameters related to charge mobility and dielectric constant, are consistent with the experimental results. The lower reorganization energy of SubPc might originate from its fused structure, in contrast to the conjugated backbone structure with conformational torsion points of DCV3T. Additionally, the net dipole moment in the axial direction of SubPc tends to be counterbalanced in dimer packing. On the other hand, the linear structure of DCV3T may promote a molecular packing in the linear direction, resulting to relatively high polarizability in the bulk state related to a high dielectric constant. From this systematic study combining electrical analysis and molecular simulation, it was identified key materials design points for the enhancement of frequency response in OPDs, in particular the fused aromatic rings for high mobility and the molecular geometry with

isotropic net dipole for low polarizability. This study gives thus an overview on the static and dynamic parameters to be considered for efficient organic color-sensitive OPD aiming at an artificial eye.

IV.5. Bibliography

1. Morimune, T.; Kajii, H.; Ohmori, Y. *IEEE Photon. Tech. Lett.* **2006**, *18*, 2662-2664.

2. Lee, K. –H.; Leem, D. –S. Castrucci, J. S. Park, K. –B.; Bulliard, X.; Kim, K. –S.; Jin, Y. W.; Lee, S.; Bender, T. P.; Park, S. Y. *ACS Appl. Mater. & Interfaces* **2013**, *5*, 13089-13095.

3. Uhrich, C.; Schueppel, R.; Petrich, A.; Pfeiffer, M.; Leo, K.; Brier, E.; Kilickiran, P.; Baeuerle, P. *Adv. Funct. Mater.* **2007**, *17*, 2991-2999.

4. Fitzner, R.; Reinold, E.; Mishra, A.; Mena-Osteritz, E.; Ziehlke, H.; Körner, C.; Leo, K.; Riede, M.; Weil, M.; Tsaryova, O.; Weiß, A.; Uhrich, C.; Pfeiffer, M.; Bäuerle, P. *Adv. Funct. Mater.* **2011**, *21*, 897-910.

5. Morse, G. E.; Bender, T. P. *ACS Appl. Mater. & Interfaces* **2012**, *4*, 5055-5068.

6. Fulford, M. V.; Jaidka, D.; Paton, A. S.; Morse, G. E.; Brisson, E. R. L.; Lough, A. J.; Bender, T. P. *J. Chem. Eng. Data* **2012**, *57*, 2756-2765.

7. Dennler, G.; Scharber, M. C.; Brabec, C. *Adv. Mater.* **2009**, *21*, 1323−1338.

8. Zou, Y.; Holmes, R. J. *Appl. Phys. Lett.* **2013**, *103*, 053302.

9. Baierl, D.; Pancheri, L.; Schmidt, M.; Stoppa, D.; Betta, G. –F. D.; Scarpa, G.; Lugli, P. *Nature Comm.* **2012**, *3*, 1175.

10. Arredondo, B.; de Dios, C.; Vergaz, R.; Criado, A. R.; Romero, B.; Zimmermann, B.; Würfel, U. *Org. Electron.* **2013**, *14*, 2484-2490.

11. Tripathi, D. C.; Tripathi, A. K.; Mohapatra, Y. N. *Appl. Phys. Lett.* **2011**, *98*, 033304.

12. Lampert, M. A.; Mark, P. *In Current Injection in Solids* Academic, New York, **1970**.

13. Tsai, W. –W.; Chao, Y. –C.; Chen, E. –C.; Zan, H. –W.; Meng, H. –F.; Hsu, C. –S. *Appl. Phys. Lett.* **2009**, *95*, 213308.

14. Brédas, J. –L,; Beljonne, D.; Coropceanu, V.; Cornil, J. *Chem. Rev.* **2004**, *104*, 4971-5003.

15. Brédas, J. –L,; Calbert, J. P.; da Silva Filho, D. A.; Cornil, J. *Proc. Nat. Aca. Sci.* **2002**, *99*, 5804-5809.

16. Sokolov, A. N.; Atahan-Evrenk, S.; Mondal, R.; Akkerman, H. B.; Sánchez-Carrera, R. S.; Granados-Focil, S.; Schrier, J.; Mannsfeld, S. C. B.; Zoombelt, A. P.; Bao, Z.; Aspuru-Guzik, A. *Nature Comm.* **2011**, *2*, 437.

17. Yang, X.; Wang, L.; Wang, C.; Long, W.; Shuai, Z. *Chem. Mater.* **2008**, *20*, 3205-3211.

18. Geng, H.; Niu, Y.; Peng, Q.; Shuai, Z.; Coropceanu, V.; Brédas, J. –L. *J. Chem. Phys.* **2011**, *135*, 104703.

19. Maex, K.; Baklanov, M. R.; Shamiryan, D.; Iacopi, F.; Brongersma, S. H.; Yanovitskaya, Z. S. *J. Appl. Phys.* **2003**, *93*, 8793-8841.

20. Klasen, M.; Bremer, M.; Gotz, A.; Manabe, A.; Naemura, S.; Tarumi, K. *Jap. J. Appl. Phys.* **1998**, *37*, L945-L948.

21. Gaussian 09, Revision C.01, Frisch, M. J.; Trucks, G. W.; Schlegel, H. B.; Scuseria, G. E.; Robb, M. A.; Cheeseman, J. R.; Scalmani, G.; Barone, V.; Mennucci, B.; Petersson, G. A.; Nakatsuji, H.; Caricato, M.; Li, X.; Hratchian, H. P.; Izmaylov, A. F.; Bloino, J.; Zheng, G.; Sonnenberg, J. L.; Hada, M.; Ehara, M.; Toyota, K.; Fukuda, R.; Hasegawa, J.; Ishida, M.; Nakajima, T.; Honda, Y.; Kitao, O.; Nakai, H.; Vreven, T.; Montgomery, J. A., Jr.; Peralta, J. E.; Ogliaro, F.; Bearpark, M.; Heyd, J. J.; Brothers, E.; Kudin, K. N.; Staroverov, V. N.; Kobayashi, R.; Normand, J.; Raghavachari, K.; Rendell, A.; Burant, J. C.; Iyengar, S. S.; Tomasi, J.; Cossi, M.; Rega, N.; Millam, N. J.; Klene, M.; Knox, J. E.; Cross, J. B.; Bakken, V.; Adamo, C.; Jaramillo, J.; Gomperts, R.; Stratmann, R. E.; Yazyev, O.; Austin, A. J.; Cammi, R.; Pomelli, C.; Ochterski, J. W.; Martin, R. L.; Morokuma, K.; Zakrzewski, V. G.; Voth, G. A.; Salvador, P.; Dannenberg, J. J.; Dapprich, S.; Daniels, A. D.; Farkas, O.; Foresman, J. B.; Ortiz, J. V.; oslowski, J.; Fox, D. J. Gaussian, Inc., Wallingford CT, **2009**.

22. Gonzalez-Rodrıguez, D.; Torres, T.; Olmstead, M. M.; Rivera, J.; Herranz, M. A.; Echegoyen, L.; Castellanos, C. A.; Guldi, D. M. *J. Am. Chem. Soc.* **2006**, *128*, 10680-10681.

23. Materials Studio, Version 7.0, Accelrys Software Inc., San Diego, CA, **2013**.

24. Fan, C. F.; Olafson, B. D.; Blanco, M.; Hsu, S. L. *Macromolecules* **1992**, *25*, 3667-3676.

25. Blanco, M. *J. Comput. Chem.* **1991**, *12*, 237-247.

26. Arago, J.; Viruela, P. M.; Gierschner, J.; Ortı, E.; Milian-Medina, B. *Phys. Chem. Chem. Phys.* **2011**, *13*, 1457-1465.

Curriculum vitae

Lee Kwag-Hee

Department of Materials Science and Engineering
College of Engineering, Seoul National University
Kwanak-ro 1, Kwanak-Gu
Seoul 151-742, KOREA
Phone: 82-2-880-7479
e-mail: photon00@snu.ac.kr

EDUCATION:

9/2005-2/2015 **Seoul National University**, Seoul, KOREA
Ph.D in Materials Science and Engineering

3/1996-2/1998 **Sung Kyun Kwan University**, Suwon, KOREA
Master of Science in Chemical Engineering
Thesis: Studies on the removal of H_2S using an optical-fiber in a bioreactor
Advisor: Professor Byoung Woo Kim

3/1992-2/1996 **Sung Kyun Kwan University**, Suwon, KOREA
B.S Degree in Chemical Engineering

INDUSTRIAL WORK EXPERIENCES:

2/1998-10/2001 **Samsung Electronics**, Yong-in, KOREA
Process Architecture of SRAM Integration in Memory business unit

11/2001- present **Samsung Advnced Institute of Technology**, Suwon, KOREA

Member of Research Staff

RESEARCH EXPERIENCES:

· Low dielectric (low-k) materials using silsesquioxane derivatives with a nanoporous structure (11/2001 ~ 2/2004)

· Organic memory using organo-metallic polymer or dendrimer (3/2004 ~ 2/2007)

· Thin film encapsulation and barrier film in organic/inorganic multilayer structures using low-temp. thermosetting silsesquioxane polymer (3/2007 ~ 2/2009)

· The transparent metal-oxide TFT using InZnO derivatives (3/2009 ~ 12/2010)

· The organic photodetector for CMOS image sensors (1/2011 ~ present)

초 록

빛을 감지하여 전기 신호를 발생하는 광감지 소자(photodetector device)는 군사 기기, 의료 기기, 이미지 센서(image sensor), 적외선 감지센서 등의 다양한 분야에서 응용이 확대되고 있다. 특히 가시광 영역의 color를 감지하여 신호를 만들어 내는 이미지 센서는 최근 모바일 기기에 탑재되는 카메라의 발전에 힘 입어 연구개발이 가속화되고 있다. 현재까지는 Si을 기반으로 한 CMOS 이미지 센서가 가장 널리 이용되고 있으며, 높은 광전 변환 효율과 낮은 누설 전류, 우수한 반도체 공정 호환성의 장점을 가져 고감도, 고해상도를 목표로 기술 개발을 주도하여왔다. 그러나, 낮은 광흡수계수와 가시광의 전체파장을 흡수하는 특성은 별도의 color-filter를 필요로 하며, 소자의 두께를 수 um로 높여야 하는 문제점으로 인해 고감도, 고집적화에 대한 기술적 한계에 도달하고 있다.

높은 흡수계수를 갖고 가시광 내에서 특정 파장영역만을 흡수하는 저분자 유기 반도체 재료는 Si 이미지 센서 분야에서 기술적 한계를 극복할 수 있는 가능성을 제시한다. 특히, 녹색 감지 특성을 갖는 유기 광전 재료를 적용한 소자를 기존의 청색과 적색 Si 광전소자 위에 적층하여 2층 배열을 할 경우, 삼색의 소자를 단층 배열하는 경우에 비하여 2배의 면적 증가 효과가 있어 감도가 2배 향상될 수 있다. 이러한, 성능 향상의 가능성을 바탕으로, 본 연구에서는 가시광 영역 중에서 특히 녹색 감지 특성을 갖는

유기반도체 재료들을 이용한 광전소자의 특성을 고찰하였다.

저분자 유기 광전변환 소자에서 널리 사용되고 있는 n형 재료는 풀러렌(Fulluerene; C60)으로서 전자 이동도가 높고 구형 구조로 인한 비정질 혼합특성이 우수하여 가장 널리 사용되어 왔다. 그러나, 가시광 영역 전반에서 흡수가 넓고 특히 청색의 흡수가 가장 높아서 녹색 광감지 소자에 적용하기에는 적합하지 않다. 따라서, 본 연구에서는 녹색 감지 소자에 적절한 흡수 파장범위를 갖는 저분자 유기 반도체 재료들의 p/n 재료의 조합 및 혼합에 의한 특성 변화로부터 바람직한 분자구조의 설계 방향을 제시하고자 하였다. 또한, 광전변환 효율, 파장 선택적 감도 및 응답 특성에 영향을 주는 전기적/물리적 제어 요소들을 살펴보았다.

제 2장에서는 녹색만 선택적으로 흡수하는 p형재료 (DMQA)와 n형재료 (DCV3T)를 가지고 bulk heterojunction (BHJ)의 구조를 갖는 녹색감지형 유기 포토다이오드를 형성하여, 5V 인가 시 540nm 파장영역에서 최대 외부양자효율 67%를 확인하였다. 높은 양자효율을 갖기 위해서는, 흡수계수와 광전자 분리 효율(photo-generated charge carrier yield)이 중요하며, BHJ에 의한 계면형성과 계면까지 도달한 엑시톤(exciton)의 전자-정공의 분리를 용이하게 하기 위하여 본 재료조합에서는 p-n 재료의 1:1 조성비에서 효율이 극대화됨을 확인하였다.

또한, 파장 선택성이 우수한 고감도 광전소자를 얻기 위해서는 목표색의 흡수계수가 높고 흡수 반치폭이 좁은 재료의 선정과 p-n 재료 조합에서

광전변환 효율을 극대화하는 것이 중요하다. 제 3장에서는 녹색 감지형 유기반도체 재료로서 subphthalocyanine 유도체들을 이용하여 우수한 파장 선택성과 높은 외부양자효율을 갖는 재료조합을 탐색하였고, spectral crosstalk을 제어하였다. 다양한 녹색감지 유기반도체 재료 중 p형으로 DMQA를 사용하고, n형으로 SubPc-Cl을 사용하여 5V 인가 시 최대 외부양자효율 60.1%를 확인하였으며, 청색의 spectral crosstalk을 0.42로 가장 낮게 제어하였다.

유기 광전소자가 이미지 센서에 적용되기 위해 응답속도는 매우 중요한 요소이다. 제 4장에서는 유사한 광전변환 효율을 갖는 DMQA/DCV3T 조합과 DMQA/SubPc 조합의 2종 광전변환 소자에서, 주파수 응답특성은 -5V 인가 시 92.9 kHz와 148.3 kHz로서 차이가 있음을 확인하였다. 소자의 동역학적 특성에 영향을 주는 인자로서 이동도와 유전율을 impedance analysis를 통해 비교, 분석하였다. 재료의 고유한 특성인 이동도와 유전율은 분자 구조에 기반한 기하학적 구조 및 fused conjugation에 의하여 달라지는 것을 분자계산을 통해 밝혀내었다.

위에서 살펴본 바와 같이, 녹색 감지특성을 갖는 유기 광전변환 재료 및 소자의 특성 고찰을 통하여 알게 된 종합적인 결과들은, 청색 또는 적색 감지형 소자의 특성 향상을 위해서도 적용될 수 있을 것이다. 따라서, 본 연구 방향 및 결과를 바탕으로 향후에는 삼원색 각각의 파장 선택적 감지 특성이 뛰어난 유기 광전소자를 3층 적층하므로써 면적이 3배 향상하고

따라서 감도도 3배 향상된 이미지 센서가 개발되기를 기대한다.

주요어: 이미지 센서, 녹색 감지형, 유기 포토 다이오드, 유기 광전변환 소자

학 번: 2005-31024

List of Publications

Original Papers

1. **Kwang-Hee Lee**, Dong-Seok Leem, Soohwan Sul, Kyung-Bae Park, Seon-Jeong Lim, Hyouksoo Han, Kyu-Sik Kim, Yong Wan Jin, Sangyoon Lee and Soo Young Park, "High performance green-sensitive organic photodiode comprising a bulk heterojunction of dimethyl-quinacridone and dicyanovinyl terthiophene", *J. Mater. Chem. C*, **2013**, 1, 2666-2671.

2. **Kwang-Hee Lee**, Dong-Seok Leem, Jeffrey S. Castrucci, Kyung-Bae Park, Xavier Bulliard, Kyu-Sik Kim, Yong Wan Jin, Sangyoon Lee, Timothy P. Bender and Soo Young Park, " Green-Sensitive Organic Photodetectors with High Sensitivity and Spectral Selectivity Using Subphthalocyanine Derivatives", *ACS Appl. Mater. Interfaces*, **2013**, 5, 13089-13095.

4. **Kwang-Hee Lee**, Gae Hwang Lee, Dong-Seok Leem, Jiyoul Lee, Jong Won Chung, Xavier Bulliard, Hyeonho Choi, Kyung-Bae Park, Kyu-Sik Kim, Yong Wan Jin, Sangyoon Lee and Soo Young Park, "Dynamic Characterization of Green-Sensitive Organic Photodetectors Using Nonfullerene Small Molecules: Frequency Response Based on the Molecular Structure", *J. Phys. Chem. C*, **2014**, 118, 13424-13431.

List of Presentations in International Conferences

1. **Kwang-Hee Lee**, Dong-Seok Leem, Kyung-Bae Park, Seon-Jeong Lim, Yong Wan Jin, Sangyoon Lee, Kyu-Sik Kim and Soo Young Park, "Green-color selective organic photodetector with high sensitivity for image sensor application" 222nd ECS PRiME 2012 (Pacific Rim Meeting on Electrochemical and Solid-State Science), October 7-12, **2012**, Honolulu, Hawaii, USA

2. **Kwang-Hee Lee**, Dong-Seok Leem, Changhoon Jung, Kyung-Bae Park, Seon-Jeong Lim, Xavier Bulliard, Kyu-Sik Kim, Yong Wan Jin, Sangyoon Lee and Soo Young Park, "Green-sensitive organic photodetector with high spectral sensitivity for image sensor application" 224th ECS Meeting, October 27-November 1, **2013**, San Francisco, California, USA